Astronomy & Astrophysics

Testing reflection features in 4U 1705−44 with *XMM-Newton*, *BeppoSAX*, and RXTE in the hard and soft states

E. Egron[1], T. Di Salvo[2], S. Motta[3,4], L. Burderi[1], A. Papitto[5], R. Duro[6], A. D'Aì[2], A. Riggio[1,7], T. Belloni[3], R. Iaria[2], N. R. Robba[2], S. Piraino[8,9], and A. Santangelo[9]

[1] Dipartimento di Fisica, Università degli Studi di Cagliari, SP Monserrato-Sestu, KM 0.7, 09042 Monserrato, Italy
  e-mail: elise.egron@dsf.unica.it
[2] Dipartimento di Fisica, Università di Palermo, via Archirafi 36, 90123 Palermo, Italy
[3] INAF – Osservatorio Astronomico di Brera, via E. Bianchi 46, 23807 Merate (LC), Italy
[4] Università dell' Insubria, via Valleggio 11, 22100 Como, Italy
[5] Institut de Ciències de l'Espai (IEEC-CSIC), Campus UAB, Fac. de Ciències, Torre C5, parell, 2a planta, 08193 Barcelona, Spain
[6] Dr. Karl Remeis-Sternwarte and Erlangen Centre for Astroparticle Physics, Friedrich-Alexander-Universität Erlangen-Nürnberg, Sternwartstrae 7, 96049 Bamberg, Germany
[7] INAF – Osservatorio Astronomico di Cagliari, Poggio dei Pini, Strada 54, 09012 Capoterra (CA), Italy
[8] INAF – IASF di Palermo, via Ugo La Malfa 153, 90146 Palermo, Italy
[9] Institut für Astronomie und Astrophysik, Kepler Center for Astro and Particle Physics, Sand 1, 72076 Tübingen, Germany

ABSTRACT

We use data from the bright atoll source 4U 1705−44 taken with *XMM-Newton*, *BeppoSAX*, and RXTE both in the hard and in the soft state to perform a self-consistent study of the reflection component in this source. Although the data from these X-ray observatories are not simultaneous, the spectral decomposition is shown to be consistent among the different observations, when the source flux is similar. We have therefore selected observations performed at similar flux levels in the hard and soft states to study the spectral shape in these two states in a broad-band (0.1−200 keV) energy range, with good energy resolution, and using self-consistent reflection models. These reflection models provide a good fit for the X-ray spectrum both in the hard and in the soft state in the whole spectral range. We discuss the differences in the main spectral parameters we find in both states, providing evidence that the inner radius of the optically thick disk slightly recedes in the hard state.

Key words. line: formation – line: identification – stars: neutron – stars: individual: 4U 1705-44 – X-rays: binaries – X-rays: general

1. Introduction

The X-ray emission in low-mass X-ray binaries (LMXBs) comes from the gravitational potential energy released from accretion processes onto black holes or neutron stars. The X-ray spectrum is generally described well by a soft-thermal component such as a blackbody or a multicolor-disk blackbody, originating in the accretion disk, and a hard X-ray component that usually dominates the spectrum. This hard component can be fitted either by a power law with a high-energy cutoff or a unsaturated Comptonization spectrum, when the source is in the so-called hard state, or by a blackbody or a saturated Comptonization spectrum, when the source is in the soft state, where the temperature of the photons is very similar to the electron temperature. The hard component is generally explained in terms of inverse Compton scattering, where soft thermal photons get Compton upscattered by hot electrons forming a corona or a boundary layer between the neutron star surface and the accretion disk, or forming the base of a jet (at least in the hard state, Markoff & Nowak 2004; Markoff et al. 2005).

In addition to this, a broad iron line (associated to the Fe Kα emission) is often detected in the spectra of X-ray binaries. However, the nature of its large width and the (a)symmetric profile of the line are still being debated. In analogy with systems containing stellar mass or supermassive black holes, which show remarkably similar phenomenology

(e.g. Martocchia & Matt 1996; Walton et al. 2012), it can be produced by reflection in the accretion disk (Reynolds & Nowak 2003; Fabian & Miniutti 2005; Matt 2006), or it can arise from an accretion disk corona (Kallman & White 1989; Vrtilek et al. 1993).

The first scenario implies that the iron line is produced in the inner part of the accretion disk. Hard X-rays coming from the corona or from the base of the jet irradiate the relatively cold accretion disk. As a consequence, a broad and asymmetric line is expected due to Doppler and relativistic effects produced close to the compact object. Depending on the ionization state of the disk, this leads to the emission of several emission lines and absorption edges that are more or less strong in the spectrum, depending on the relative abundance of the corresponding ion and/or its fluorescence yield (Kaastra & Mewe 1993). The Fe Kα line at 6.4−7 keV is the most prominent feature (Fabian et al. 2000). It results in a fluorescent line at 6.40 keV from Fe I-XVII or in the recombination lines at 6.67−6.70 keV and 6.95−6.97 keV associated with highly ionized species of Fe XXV (He-like) and Fe XXVI (H-like), respectively. In this scenario other reflection signatures are also expected, such as the emission and/or absorption from several elements at lower energy, and a Compton reflection hump at higher energy (George & Fabian 1991; Ballantyne et al. 2001; Ross & Fabian 2007) if the X-ray continuum spectrum is sufficiently hard.

D'Aì et al. (2009), Iaria et al. (2009), Di Salvo et al. (2009), and Piraino et al. (2012) detect emission lines in GX 340+0, GX 349+2, 4U 1705−44, and GX 3+1 at 2.6, 3.31, and 3.90 keV associated with S XVI, Ar XVIII, and Ca XIX, respectively, and an absorption edge from ionized iron. Moreover, a reflection hump peaking at nearly 30 keV has been found in several sources, such as 4U 1705−44 (Fiocchi et al. 2007). To confirm the common origin of these features, it is important to use self-consistent models that include all the reflection components in order to distinguish among the proposed production mechanisms.

Alternative scenarios explain the line broadening by Compton scattering if the line is emitted in the inner parts of a moderately optical thick accretion disk corona (ADC), formed by evaporation of the outer layers of the disk (White & Holt 1982). Another possibility is that the line profile is red-skewed due to Compton upscattering by a narrow wind shell launched at mildly relativistic velocities at some disk radii where the local radiation force exceeds the local disk gravity (Titarchuk et al. 2009).

Thanks to the good energy resolution capabilities of *Chandra* and to the large effective area of *XMM-Newton* and *Suzaku*, the number of significant detections of these lines is increasing, giving the possibility to study their profile in more detail. Recently, two studies have been performed by Ng et al. (2010) and Cackett et al. (2010) to investigate the nature of the iron line with a large sample of neutron star LMXBs spectra. Using *XMM-Newton* observations of 16 neutron star LMXBs, Ng et al. (2010) conclude that there is no statistical evidence that the iron line profile is asymmetric, and they propose that the observed large width of the line is caused by Compton scattering in the corona. It should be noted that, to eliminate the effects of photon pile-up in the *XMM-Newton* data, Ng et al. (2010) decided to reject up to 90% of the source photons for the brightest sources. Conversely, by studying ten neutron star LMXBs with *Suzaku* (which is less affected by photon pile-up because of a broad point spread function) and *XMM-Newton*, Cackett et al. (2010) confirm that the Fe line is asymmetric, relativistic, and produced by reflection in the inner part of the accretion disk. This result was also achieved by comparing CCD-based spectra from *Suzaku* with Fe K line profiles from archival data taken with gas-based spectrometers Cackett et al. (2012). In general, they find good consistency between the gas-based line profiles from EXOSAT, *BeppoSAX*, RXTE, and the CCD data from *Suzaku*, demonstrating that the broad profiles they see are intrinsic to the line and not because of instrumental issues.

The low-mass X-ray binary system 4U 1705−44 contains a weakly magnetized neutron star. In such systems the accretion disk can extend down to the neutron star surface. This implies a similar configuration with respect to the one envisaged for accreting black holes, since the radius of the neutron star is close to the size of the innermost stable circular orbit (ISCO) of matter around a black hole. Similarities have been observed between these systems (e.g., Maccarone 2012, and references therein), suggesting common physical processes producing X-ray emission and similar properties of the accretion flow around the compact object. Clear observational evidence exists that a neutron star has a solid surface, such as the observations of type I X-ray bursts, which are thermonuclear explosions in the surface layers of the neutron star, or of coherent pulsations, resulting from the magnetic field anchored on the neutron star surface. However, not all systems containing a neutron star show one or more of these characteristics (Done et al. 2007).

4U 1705−44 is a persistent bright source that shows type I X-ray burst (Langmeier et al. 1987) and kHz quasi-periodic oscillations (Ford et al. 1998; Olive et al. 2003). From some bursts that show photospheric radius expansion, its distance is estimated at 7.4 kpc, toward the Galactic ridge (Forman et al. 1978; Galloway et al. 2008).

LMXBs containing a neutron star are divided into two categories (Hasinger & van der Klis 1989) according to the path the source describes in the X-ray color-color diagram (CD) or hardness-intensity diagram (HID): atoll sources (C-like, low luminosity, about $0.001−0.5\,L_{\rm Edd}$) or Z-sources (Z-like, high luminosity, close to the Eddington limit). 4U 1705−44 is classified as an atoll source. In the classical CD pattern of these sources, two branches are usually distinguished: the island and the banana. In the island branch, the source presents a low count rate, probably associated to a low-mass accretion rate, and the source is in the low/hard state (low is relative to the X-ray flux, and hard to the spectrum). In this state, it is thought that the accretion disk is truncated relatively far from the compact object. This results in a very hot corona and in a hard spectrum. On the other hand, when the source is in the banana branch, the accretion disk approaches the compact object, the temperature of the corona decreases due to Compton cooling, and the source is in the high/soft state. The mass accretion rate is therefore expected to increase from the island to the banana branch. The Z-sources usually emit persistently at high luminosity and are thought to have a larger magnetic field and/or higher mass accretion rate than atoll sources.

The system 4U 1705−44 has recently been studied thoroughly with the particular objective of understanding the origin of its iron line. A broad Fe line was clearly visible with *Chandra* (Di Salvo et al. 2005), confirming previous studies performed at low-energy resolution by White et al. (1986) and Barret & Olive (2002). The HETG onboard *Chandra* excluded that the large width of the line could be caused by the blending of lines from iron in different ionization states, although it was not possible to distinguish between the two possible origins of the line width (relativistic smearing or Compton broadening). The broad band *BeppoSAX* spectrum of 4U 1705−44 taken during a soft state again showed a broad iron line that could be well fitted by a DISKLINE component with very reasonable smearing parameters (Piraino et al. 2007), and the INTEGRAL spectrum showed clear evidence of a Compton reflection hump (Fiocchi et al. 2007), as well as the *BeppoSAX* spectrum taken during the hard state (Piraino et al., in prep.).

The observations with *XMM-Newton* and *Suzaku* were essential for studying the iron line profile in detail because of their large effective area and good energy resolution. Indeed, Reis et al. (2009b) found a broad (skewed) and asymmetric Fe Kα emission line during a *Suzaku* observation of 4U 1705−44. Both Compton broadening and relativistic smearing were needed to account for the large width of the iron line. The best fit value of the inner radius was $R_{\rm in} \simeq 10.5\,R_{\rm g}$, with $R_{\rm g}$ being gravitational radius ($R_{\rm g} = GM/c^2$), and the corresponding inclination angle was $i \sim 30°$. Using the observations from *BeppoSAX* and *Suzaku*, Lin et al. (2010) obtained constraints on the broad-band spectrum of 4U 1705−44 and find that the strength of the Fe line correlates well with the boundary layer emission in the soft state, while the Fe line is probably due to illumination of the accretion disk by the strong Comptonization emission in the hard state. An *XMM-Newton* observation performed in 2008 when the source was in a soft state confirmed the results obtained with *Suzaku*, showing a high-statistics Fe line profile and spectrum consistent with a disk-reflection scenario (Di Salvo et al. 2009; D'Aì et al. 2010). The best fit value of the
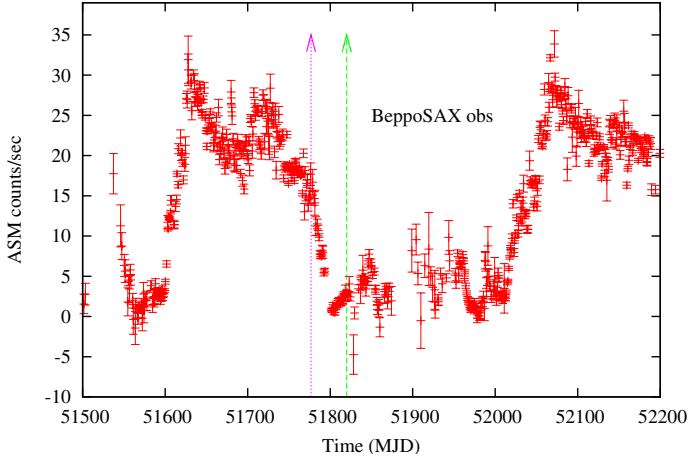
Fig. 1. Light curve of 4U 1705-44 obtained with RXTE/ASM from November 1999 to October 2001. The two arrows show the observations performed by *BeppoSAX* in August and October 2000.

Fig. 2. RXTE/ASM light curve of 4U 1705-44 from May 2005 to November 2010. The arrows mark the two *XMM-Newton* observations performed in August 2006 and 2008. The black crosses and the blue triangles represent the RXTE observations selected in the hard and soft states, respectively.

inner disk radius was $R_{in} \simeq 14\, R_g$ and the corresponding inclination angle and index of the emissivity law profile were $i \sim 39°$ and -2.3 respectively, in agreement with the *Suzaku* results. In addition, the *XMM-Newton* spectrum shows the presence of several emission lines from elements lighter than iron, such as S, Ar, and Ca at 2.62 keV, 3.31 keV, and 3.90 keV, respectively, and an absorption edge at 8.5 keV probably from ionized iron. All these features were broad and consistent with being produced in the same region where the iron line was produced.

Here we present the spectral analysis of 4U 1705−44 using data from *XMM-Newton*, *BeppoSAX*, and RXTE when the source was both in the hard state and in the soft state. Using the same spectral models to describe the source spectrum in both states, we aim at highlighting the differences in the spectral parameters to find that the accretion disk is truncated farther (but not far) from the compact object in the hard state. Since several reflection features have been detected in 4U 1705−44, we use self-consistent reflection models to fit the broad-band, multimission, X-ray spectrum of this source. We also discuss possible effects of pile-up distortion in the *XMM-Newton* spectrum during the high-luminosity, soft state.

2. Observation and data reduction

The light curve produced from the All-Sky Monitor onboard RXTE allows following the evolution of the source flux for a period of ~16 years. The source shows clear spectral transitions, from the hard (3 counts/s) to the soft state (25 counts/s). A total of four observations were performed with *BeppoSAX* (see Fig. 1) and *XMM-Newton* (see Fig. 2) when the source was in the soft and hard states. The spectral transitions are associated with variations in the X-ray flux, which are most likely proportional to the accretion rate. We select RXTE observations, both in the hard and soft states, as shown in Fig. 2. In this way, the joint spectra from the three satellites cover the full 0.1−200 keV energy range. We explain in detail our methods in the following.

2.1. XMM-Newton

The source 4U 1705−44 was observed twice with *XMM-Newton*. The first observation was performed on 2006 August 26 for an effective exposure of 34.72 ks, when the source was in the hard state. The corresponding RXTE/ASM count rate was 1 c/s. The
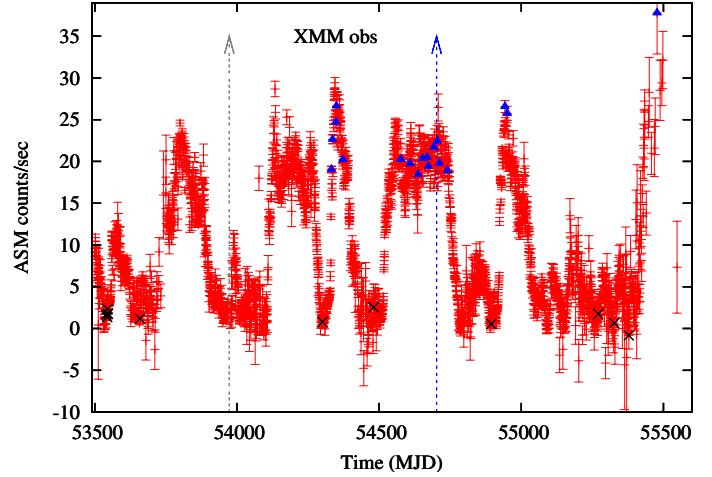
second time, 4U 1705−44 was observed during the soft state (target of opportunity), on 2008 August 24 for a total on-source observing time of 45.17 ks (see Di Salvo et al. 2009, for more details on this observation). The RXTE/ASM was 19 c/s during this observation.

During both observations, the European Photon Imaging Camera pn (EPIC-pn; Struder et al. 2001) and the Reflection Grating Spectrometers (RGS1 and RGS2; den Herder et al. 2001) were used to observe the source. The EPIC-pn camera operated in timing mode to minimize the photon pile-up and telemetry overload that may occur at high count rates, with a thick filter in place, which further reduced the number of low-energy photons. In timing mode only the central CCD is read out with a time resolution of 30 μs. This provides a one-dimensional image of the source with the second spatial dimension being replaced by timing information. The EPIC-MOS and the optical Monitor were off during the second observation in order to avoid telemetry drop-outs in the EPIC-pn.

We produced a calibrated photon event file using the SAS[1] processing tool EPPROC. Before extracting the spectra we checked for contamination from background solar flares by producing a light curve in the energy range 10−12 keV. No solar flare was registered. However, during the first observation (corresponding to the hard state), the EPIC-pn camera registered a type-I X-ray burst at about 11 ks after the start of the observation. We applied temporal filters by creating a good time interval (GTI) file with the task TABGTIGEN in order to remove the burst.

We used the task EPFAST to correct rate-dependent CTI effects in the event list. The source spectra were extracted from a rectangular area covering all the pixels in the Y direction and centered on the brightest RAWX column (36 in the hard state, 38 in the soft state) with a width of 16 pixels, which corresponds to 65.6 arcsec. We selected only events with PATTERN ≤ 4 (single and double pixel events) and FLAG = 0 as a standard procedure to eliminate spurious events. We extracted the background spectra from a box similar to the one used to extract the source photons but in a region away from the source (RAWX = 47−63 and RAWX = 4−12 in the hard and soft states, respectively).

During the first observation, the average count rate registered by EPIC-pn CCDs is around 48 c/s, and 19 c/s in the 2.4−11 keV range, excluding the burst interval. In the soft state, the count rate is much higher: the mean count rate of around 770 count/s, and 425 count/s in the 2.4−11 keV range, slightly increasing in time (by 5%). We also checked for the presence of pile-up using the task EPATPLOT. While the first *XMM-Newton* observation of the source taken in the hard state does not show any significant pile-up, a few percent pile-up affects the second observation taken during a soft state. We discuss the pile-up issue concerning the soft state in the next section. We grouped the EPIC-pn energy channels by a factor of 4 in order to avoid oversampling of the energy-resolution bin of the instrument.

The two RGS units were set in the standard spectroscopy mode. The RGS data were processed using the RGSPROC pipeline to produce calibrated event list files, spectra, and response matrices. The RGS data were rebinned to have at least 25 counts per energy channel.

2.2. BeppoSAX

BeppoSAX performed two observations of 4U 1705−44 in August and October 2000, for total on-source observing times of 43.5 ks and 47 ks, respectively. The count rates registered by the RXTE/ASM associated to these observations were 18 c/s and 3 c/s, respectively.

The four *BeppoSAX* narrow field instruments were on during both the observations. The Low Energy Concentrator Spectrometer (LECS, 0.1−4 keV; Parmar et al. 1997) and the Medium Energy Concentrator Spectrometer (MECS, 1−10 keV; Boella et al. 1997) data were extracted in circular regions centered on the source position using radii of 8′ and 4′, respectively, corresponding to 95% of the source flux. Identical circular regions were used in blank field observations to produce the background spectra. The background spectra of the High Pressure Proportional Gas Scintillation Counter (HPGSPC, 8−50 keV; Manzo et al. 1997) and of the Phoswich Detection System (PDS, 15−200 keV; Frontera et al. 1997) were produced from Dark Earth data and during off-source intervals. The HPGSPC and PDS spectra were grouped using a logarithmic grid.

We did not use data from PDS during the first observation, which corresponds to the soft state, in order to avoid the extra complication of the spectral fit caused by the presence of a hard (power law) spectral component (see Piraino et al. 2007). During the low/hard observation, 6 X-ray bursts were removed from the data.

2.3. RXTE

There was no simultaneous observation performed by RXTE during the *XMM-Newton* and *BeppoSAX* observations. However, the archive has provided us with hundreds of RXTE observations of 4U 1705−44 since RXTE was launched. Therefore, we considered all the observations of 4U 1705−44 collected since 2000 May (corresponding to the 5th epoch of RXTE[2]) and selected RXTE observations during which the source showed the same spectral state of the two *XMM-Newton* observations as mentioned above. To do so we produced a color-color diagram (CD) from all the RXTE observations and a time-resolved CD from the two *XMM-Newton* observations (we separated
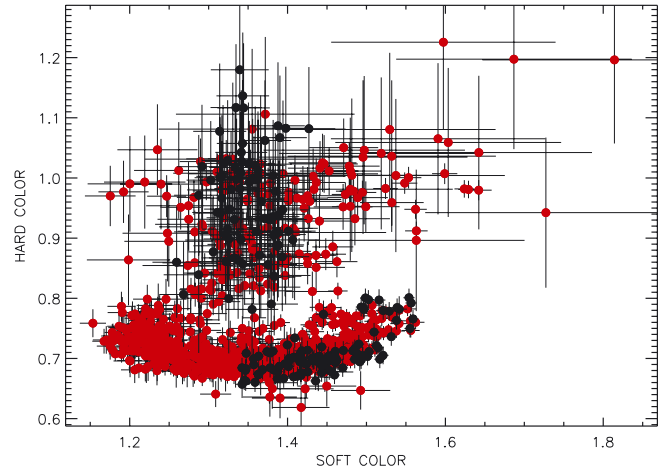
Fig. 3. Color−color diagrams (CDs) of 4U 1705−44 produced by RXTE/PCA and *XMM-Newton*/EPIC-pn, in red and black, respectively. See text for the details.

the *XMM-Newton* observations in intervals 512 s long, and for each of them, we produced a spectrum and measured the colors) using the same energy bands for the two instruments (i.e. 2.47−3.68 keV and 3.68−5.31 keV for the soft color and, 5.31−7.76 keV, 7.76−10.22 keV for the hard color). Since from the RXTE data it is clear that the shape of the CD of 4U 1705−44 remains constant during the period considered, we could directly compare the CD coming from the two instruments. The CDs were normalized to the Crab colors, but an additional correction was needed to precisely match the two diagrams and to take the differences in the gain of the two instruments into account. Figure 3 shows the *XMM-Newton* CD corresponding to the two observations performed in the hard and in the soft state superposed to the RXTE CD. Starting from the two CDs, we selected the RXTE observations that matched the *XMM-Newton* observations. The detail of the RXTE observations selected is given in Table 5.

The RXTE data were obtained in several simultaneous modes. STANDARD 2 mode for PCA and STANDARD for the HEXTE instrument were used to create background and dead-time-corrected spectra. We extracted energy spectra from PCA and HEXTE for each observation using the standard RXTE software within HEAsoft v.6.9 following the standard procedure described in the RXTE cookbook to produce source and background spectra, as well as response matrices. Only Proportional Counter Unit 2 from the PCA was used, since only this unit was on during all the observations. As regards HEXTE data, we used only data coming from HEXTE/Cluster B, which were correctly working in our period of interest.

Then we produced RXTE/PCA and RXTE/HEXTE spectra for each RXTE observation, and we averaged them to obtain a PCA+HEXTE spectrum in the island state (matching *XMM-Newton* observation made in 2006 August 26) and a PCA spectrum in the banana-state (matching *XMM-Newton* observation made in 2008 August 24). In the soft state we did not use RXTE/HEXTE data due to the lack of counts in the HEXTE working enery range (20−200 keV). A systematic error of 0.6% was added to the PCA-averaged spectra to account for residual uncertainties in the instrument calibration[3].

---

[2] We only considered data from the 5th epoch to avoid fluctuations due to the differences in the instrument gain that can be observed in data coming from different epochs.

[3] http://www.universe.nasa.gov/xrays/programs/rxte/pca/doc/rmf/pcarmf-11.7 for a detailed discussion of the PCA calibration.

3. Spectral analysis

Data were fitted by using Xspec (Arnaud 1996) v.12.6. All uncertainties are given at the 90% confidence level ($\Delta\chi^2$ = 2.706). The data analysis of the XMM/EPIC-pn spectrum was restricted to 2.4−11 keV to exclude the region around the detector Si K-edge (1.8 keV) and the mirror Au M-edge (2.3 keV) that could affect our analysis. This problem has already been noticed for the EPIC-pn observations performed in timing mode (e.g., D'Aì et al. 2010; Papitto et al. 2010; Egron et al. 2011). The energy bands used for the other instruments are: 0.3−4 keV for the LECS, 1.8−10 keV for the MECS, 7−34 keV for HPGSPC, 15−200 keV for PDS onboard *BeppoSAX*, and 4−22 keV for PCA, and 15−100 keV for HEXTE onboard RXTE.

The following sections concern the analysis of data associated to the soft and to the hard state of 4U 1705−44. In the first one, we report investigation of the pile-up effects on the *XMM-Newton* data of the soft state to demonstrate that the iron line is always broad and gives consistent spectral parameters that are independent of the extraction region. Then we applied reflection models to fit the *XMM-Newton* data in this state, and finally we included the *BeppoSAX* and RXTE data to extend the analysis to the broad-band, 0.1−200 keV, energy range. In the second one, we applied the same continuum and reflection models to the *XMM-Newton*, *BeppoSAX*, and RXTE data in the hard state, in order to evaluate which spectral parameters change from one state to the other.

4. Soft state

4.1. Pile-up in XMM-Newton /EPIC-pn data?

Pile-up is an important concern for CCD data and may affect the spectral results. It occurs when more than one X-ray photon hits the same pixel or an adjacent one in the same read-out frame. If this happens the CCD will be unable to resolve the individual photon events and instead record a single event with an energy that is roughly the sum of the individual event energies. It results in a shift of the photons to higher energy, which produces an energy-dependent distortion of the spectrum. It is possible to assess the pile-up effects by checking the fraction of single, double, triple, and quadruple events (depending on how many pixels are involved) using the task EPATPLOT (see Appendix).

Di Salvo et al. (2009), D'Aì et al. (2010), and Ng et al. (2010) have studied the iron line in 4U 1705−44 using the same *XMM-Newton* data in the soft state, but considering different extraction regions for the spectra and therefore accepting different pile-up fraction in their spectral analysis. Di Salvo et al. (2009) consider that pile-up effects on spectral results were negligible and thus decided to keep all the central columns of the CCD, whereas D'Aì et al. (2010) excluded the brightest CCD column, and Ng et al. (2010) excluded seven central columns (corresponding to ∼90% of the source counts). In all these cases, the iron line detected in the pn spectra of 4U 1705−44 consistently remains broad, with a Gaussian sigma ∼0.3−0.4 keV. However, the conclusions coming from the spectral analysis differ. While Di Salvo et al. (2009) and D'Aì et al. (2010) deduce that the iron line is clearly asymmetric and compatible with a relativistic line, using the DISKLINE (Fabian et al. 1989) and the reflection model REFBB (Ballantyne 2004), respectively, Ng et al. (2010) find that the iron line can be fit equally well by a Gaussian or using the LAOR model (Laor 1991), concluding that there was no statistical evidence of any asymmetry of the line profile. It is thus important to assess the effects of pile-up in the EPIC-pn spectrum of 4U 1705−44 in the soft state, which shows the highest
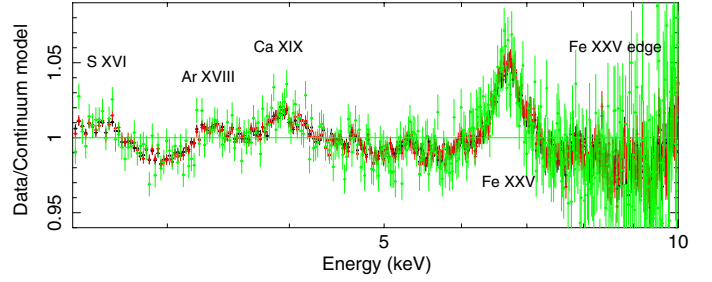
Fig. 4. Comparison of the ratios of the data to the best fit continuum considering all the rows of the CCD (black; Di Salvo et al. 2009), without the brightest CCD column (red; D'Aì et al. 2010), and excluding seven central columns (green; Ng et al. 2010). The continuum model consists of a blackbody and a Comptonization model (comptt) modified by photoelectric absorption (phabs).

signal-to-noise ratio (S/N) iron-line profile ever detected to date in a neutron star LMXB.

To evaluate the pile-up effects on the *XMM-Newton*/pn spectrum, we applied an empirical model that is similar to the one used in Di Salvo et al. (2009), to compare the results obtained when we consider different extraction regions in the CCD. In particular, we consider the extraction region described in Sect. 2, where we exclude from zero up to seven central brightest columns before extracting the pn spectrum. Figure 4 shows the ratios of the data to the continuum obtained for three cases: excluding none, one, and seven of the central brightest columns. The continuum model consists of a blackbody and a Comptonization component (COMPTT; Titarchuk 1994), modified at low energy by the photoelectric absorption (PHABS; photoelectric cross-sections of Balucinska-Church & McCammon 1992 with a new He cross-section based on Yan et al. 1998; and standard abundances of Anders & Grevesse 1989). This model is often used for atoll sources and gives a good fit for the continuum of this source (Barret & Olive 2002; Di Salvo et al. 2005; Piraino et al. 2007; Di Salvo et al. 2009).

Three emission lines are visible at low energy, at 2.62 keV, 3.31 keV, and 3.90 keV, identified by Di Salvo et al. (2009) as highly ionized elements corresponding to S XVI, Ar XVIII, and Ca XIX, respectively. In addition to these lines, an iron emission line and an absorption edge are present. The detection of the iron line is at about 10σ above the continuum when all the columns are considered, whereas it becomes only 5σ when seven columns are removed. In the three cases, the iron line appears broad and the shape is very similar. To fit these residuals we add four Gaussians and an edge to the continuum model, all modified by the same relativistic blurring (modeled with RDBLUR, the DISKLINE kernel, in Xspec) component to consider the relativistic and/or Doppler effects produced by the motion in the inner disk close to the compact object. This model describes the relativistic effects due to the motion of plasma in a Keplerian accretion disk, immersed in the gravitational well of the compact object, in terms of the inner and the outer radius of the disk, R_{in} and R_{out} (in units of the gravitational radius, $R_g = GM/c^2$, where M is the mass of the compact object), of the index of the assumed power-law dependence of the disk emissivity on the distance from the NS, and of the system inclination, *i*. In this way, all the discrete features present in the model are smeared by the same disk parameters. The only difference with respect to the model used by Di Salvo et al. (2009) is that the RDBLUR component is now also applied to the iron edge, as it should be if the edge is also produced by reflection in the same disk region as the other emission lines.

As expected, we note a variation in the parameters of the continuum when we exclude the columns from 0 to 7, the most affected parameter being the interstellar absorption column density. Its value, and the associated error, progressively increase from $(1.8 \pm 0.1) \times 10^{22}$ cm^{-2} when no central columns are excluded (pn-all) to $(3.5 \pm 0.5) \times 10^{22}$ cm^{-2} when seven central columns are excluded (pn-7). It should be noted here that the best fit value for this parameter obtained with *BeppoSAX* was $(1.9 \pm 0.1) \times 10^{22}$ cm^{-2} (Piraino et al. 2007), compatible with the results obtained for spectra pn-all to pn-2. Other significant changes in the parameter values are in the temperature and normalization of the blackbody component, with the temperature decreasing and the normalization increasing from pn-all to pn-7. Also in this case, the best fit values of these parameters obtained with *BeppoSAX* are compatible with the results obtained for spectra pn-all to pn-2. The temperature of the seed photons of the COMPTT component is quite stable, while some scattering is observed in the values of the electron temperature and optical depth of this component, although the errors are also very large. Regarding the discrete features and the disk-smearing parameters, all the values are compatible with each other within the errors, which of course increase significantly with the decreasing counts. The inclination angle is the parameter that is mostly affected by the choice of the extraction region, with values ranging from $38° \pm 1$ to $58°^{+23}_{-2}$ going from pn-all to pn-7 (the largest increase occurring starting from spectrum pn-4).

To assess whether the exclusion of some central columns of the CCD has noticeable effects on the spectral shape or simply induces a lack of statistics, we carried out the same analysis as described above, but also considering the RGS spectrum, together with the pn spectrum. The uncertainties on the column density and on the inclination decrease strongly. While the value associated to the column density remains constant, $N_{\rm H} = (1.6 \pm 0.1) \times 10^{22}$ cm^{-2}, the inclination goes from $38° \pm 1$ when no central column is excluded to $40°^{+6}_{-3}$, when seven central columns are excluded. Also, the values of the parameters such as the blackbody temperature, its normalization, and the electron temperature become much more stable, with the error bars considerably reduced. The results are summarized in Table 6. In conclusion, we checked the effect of pile-up in the EPIC-pn spectrum but excluding from none up to seven of the brightest central columns and comparing the best fit spectral parameters. The parameters seem to depend on the extraction region when looking at the EPIC-pn spectra alone. However, the addition of the RGS data clearly stabilizes the values of the parameters. This means that the variation in the parameters and in the corresponding error bars we obtain fitting the EPIC-pn spectra alone are caused by a decrease in the statistics when excluding the central columns of the CCD, hence by a lack of constraints on the parameters.

Moreover, if we look at the plots presented in Appendix, we can see that the deviation of single and double events at the iron line energy has a minimum in correspondence of the pn-2 spectrum, and it increases again when we exclude more than two brightest central columns. This may be ascribed to a mismodeling of the instrumental response and, in particular, of the rate of double events (which involve more than one pixel, and probably more than one column) when too many central columns are excluded. Although most continuum parameters obtained for spectra pn-all to pn-2 are perfectly compatible to those previously obtained with *BeppoSAX* (Piraino et al. 2007), we adopt a conservative approach for the present analysis, to minimize any residual pile-up source of uncertainty. We therefore chose to work with spectrum pn-2.

Table 1. Iron line complex in the XMM/EPIC-pn data fitted by four Gaussians corresponding to the Fe XXV triplet and the Fe XXVI line.

Fe line		Energy (keV)	σ (keV)	Norm (10^{-3} cm^{-2} s^{-1})
Fe XXV	F	6.64	$0.11^{+0.05}_{-0.11}$	$0.6^{+0.4}_{-0.5}$
	I_1	6.67	0.36 ± 0.06	2 ± 0.5
	R	6.70	$0.09^{+0.26}_{-0.09}$	$0.2^{+0.6}_{-0.2}$
Fe XXVI	Lyα_2	6.95	$0.14^{+0.12}_{-0.08}$	0.3 ± 0.2

We therefore considered the spectrum pn-2, whose continuum emission is fitted by a blackbody and a comptonized component (COMPTT), both modified at low energy by photoelectric absorption. We first added four Gaussians and an edge to the continuum model to take the emission lines at low energy (S, Ca, Ar), the iron line, and the iron edge at 8.6 keV into account. In this case, the iron line was found at 6.70 ($\pm$0.02) keV, and its equivalent width was 42 eV. The corresponding $\chi^2_{\rm red}$ was 1.14 (408).

We also tried to fit the iron line at 6.7 keV, which very likely corresponds to the Kα transition of Fe XXV, with the single components of the triplet (composed of the forbidden line at 6.64 keV, the intercombination lines at 6.67 keV and 6.68 keV, and the resonance line at 6.70 keV). We also added a line at 6.95 keV associated with emission from Fe XXVI. To do so, we used five Gaussians (instead of a single Gaussian at 6.6 keV) whose centroid energies are fixed at the expected rest-frame energies. The lines at 6.67 keV and 6.68 keV are indistinguishable with *XMM-Newton*, since the difference in the centroid energies is comparable to the fitting errors on the line energy. We therefore considered only one Gaussian at 6.67 keV to represent the intercombination lines. This line clearly dominates the triplet, although the lines at 6.64, 6.70, and 6.95 keV contribute slightly to the emission. The results are summarized in Table 1. Accordingly, we used a single Gaussian to describe the Fe complex.

Then we added a smearing component to this model to take relativistic and/or Doppler effects into account close to the compact object, in the hypothesis of a disk origin of the iron line. This component was convolved with all the four Gaussians (associated with S, Ar, Ca, and Fe) and with the edge. We froze the sigma of the Gaussians to zero and applied the same relativistic relativistic smearing parameters to all these features. The iron line is found at $6.66^{+0.01}_{-0.02}$ keV. The equivalent width is 57 eV. The inclination and the inner radius are $39°^{+2}_{-1}$ and 14^{+3}_{-2} $R_{\rm g}$, respectively. The corresponding $\chi^2_{\rm red}$ is 1.03 (409 degrees of freedom, hereafter d.o.f.), and the χ^2 decreases by $\Delta\chi^2 = 44$ for one parameter more with respect to the model without the smearing component. Therefore the addition of a mildly relativistic smearing improves the fit, favoring the interpretation of the discrete features in the pn spectrum of 4U 1705−44 as produced by reflection in the inner accretion disk. To support this interpretation, in the next section we fit the broad band (0.3−200 keV) spectrum of 4U 1705−44 in the soft and in the hard state to self-consistent reflection models.

4.2. Reflection models on pn-2

To test that the iron line, the edge, and the three low-energy emission lines (S XVI, Ar XVIII, and Ca XIX) are consistent with

a reflection scenario, we applied the self-consistent reflection model REFLIONX on the *XMM-Newton*/pn spectrum. REFLIONX is a self-consistent model that includes both the reflection continuum and the corresponding discrete features (Ross & Fabian 2005). In addition to fully-ionized species, the following ions are included in the model: C III-VI, N III-VII, O III-VIII, Ne III-X, Mg III-XII, Si IV-XIV, S IV-XVI, and Fe VI-XXVI. However, it does not include Ar XVIII and Ca XIX. We therefore added two Gaussians to take the emission lines from these two elements into account. We multiplied REFLIONX by a high-energy cutoff (modeled with HIGHECUT in xspec), where the cutoff energy was frozen to 0.1 keV and the folding energy was fixed to be 2.7 times the temperature of the electrons. In fact, for a saturated Comptonization, a Wien bump is formed at the electron temperature, whose peak is at about three times the electron temperature. We used NTHCOMP (Zdziarski et al. 1996; Zycki et al. 1999) to model the Comptonization continuum instead of COMPTT in order to have the photon index Γ as the fitting parameter of the continuum. Its value was fixed to be equal to the photon index of the illuminating component in the reflection model. The χ^2/d.o.f. obtained with this model is 577/413 (~1.40).

To take the smearing of the reflection component induced by Doppler and relativistic effects into account in the inner disk close to the compact object, we convolved the reflection model and the two Gaussians with the same RDBLUR component. This gives as best fit parameters the inclination of the system ($38^{\circ+2}_{-1}$), the inner and outer radii of the accretion disk ($R_{in} = 13^{+4}_{-6}$ and R_{out} is fixed at 3500 R_g), and the index of the emissivity law profile (-2.2 ± 0.1). We froze the width of the Gaussian lines at 0 keV to apply the same smearing parameters applied to the RE-FLIONX component. The χ^2/d.o.f. is 523/412 ($\Delta\chi^2 \sim 54$ for the addition of 1 parameter; the corresponding F-test probability of chance improvement is 2×10^{-10}). This attests that the RDBLUR component is statistically required to improve the fit. However, the reflection component does not seem to fit the iron edge correctly, since some features are still present in the residuals at about 8.5 keV. We added an edge to the model, also convolved with the same RDBLUR component (under the assumption that the edge is also produced in the same region of the accretion disk as the reflection component). The edge is found at 8.7 keV and the associated depth is 0.06. The χ^2 decreases by 83 for the addition of two parameters, resulting in a $\chi^2_{red} = 1.07$ (410).

To check the consistency of the edge with the reflection continuum, we used another reflection model, PEXRIV (Magdziarz & Zdziarski 1995), which includes the iron edge and the Compton bump of the reflection component. This model consists in an exponentially cutoff power-law spectrum reflected by ionized material; however, this model does not include any emission lines, so four Gaussians (S, Ar, Ca and Fe) were added and convolved, together with the pexriv component, with the RD-BLUR component. The photon index of PEXRIV is fixed to the one obtained with the NTHCOMP model, and the cutoff energy is 2.7 times the electron temperature obtained with NTHCOMP. The normalization of the PEXRIV model was fixed to the one of the cutoff power-law model included in NTHCOMP. To do so, we applied a cutoff power-law model to the data and calculated the normalization in such a way that the bolometric flux is the same as with NTHCOMP. The χ^2_{red} obtained with this model is 1.06 (410 d.o.f.). The values of the smearing parameters agree with the previous model, and the features at about 8.5 keV are no longer visible in the residuals, so the edge is well fit by PEXRIV and is likely a reflection feature. However, it is not well fit by the REFLIONX component.
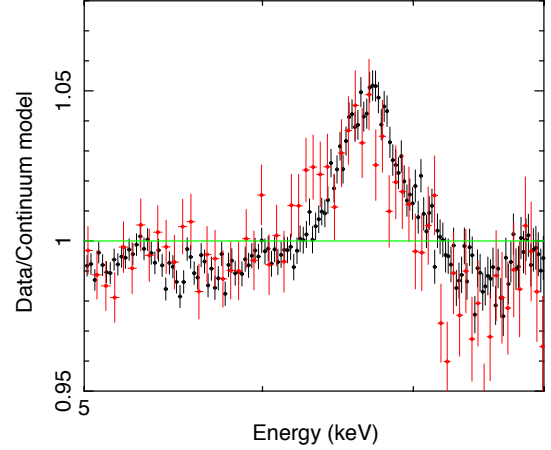
Fig. 5. Ratio of the data to the continuum model for XMM/EPIC-pn (black) and *BeppoSAX*/MECS (red) in the energy range 5−8 keV showing the broad iron line clearly visible in both spectra, although the statistics are much better in the case of the pn spectrum. The continuum is described by the spectral model phabs (bbody + compTT) in Xspec.

4.3. Reflection models on the XMM-Newton, BeppoSAX, and RXTE data

Considering the data of *XMM-Newton* and *BeppoSAX* separately, the continuum of these spectra is well fit by a blackbody plus a thermal Comptonized model (COMPTT or NTHCOMP) modified at low energy by the interstellar photoelectric absorption (PHABS). In both cases, the fit is improved by adding a broad iron line, fitted by a Gaussian line or, even better, by a DISKLINE. The best fit parameters, obtained by fitting the spectra from the two different X-ray observatories separately, are similar to each other and agree with previous results reported by Piraino et al. (2007) and Di Salvo et al. (2009) on 4U 1705−44. Regarding the *BeppoSAX* data, the absorption column density is $N_H = 1.4 \times 10^{22}$ cm^{-2}, the blackbody temperature is 0.56 keV, and the temperatures of the electrons and of the seed photons of the Comptonized component are 3.5 keV and 1.2 keV, respectively. A diskline is found at 6.8 keV, the inclination of the system is $28^{\circ+8}_{-5}$, and the inner radius is about 8^{+4}_{-2} R_g. The χ^2/d.o.f. corresponding to this fit is 584/503 ($\chi^2_{red} \sim 1.16$). This is better than using a Gaussian to fit the iron line (χ^2/d.o.f. is 618/505, $\chi^2_{red} \sim 1.23$; an F-test gives a probability of chance improvement of about 10^{-6}). These results agree perfectly with the results we obtain from the *XMM-Newton* spectrum, independently of the particular model we used to fit the reflection features; however, the uncertainties on the inner radius and on the inclination angle are larger than in the case of *XMM-Newton*. This can be explained by the quality of the data, which is better in the case of *XMM-Newton* thanks to its larger effective area and higher resolution capabilities. In Fig. 5 we show the ratio of the data to the best-fit continuum model in the energy range 5−8 keV to compare the residuals at the iron line as observed by the *XMM-Newton*/EPIC-pn and by the *BeppoSAX*/MECS. The iron line profile appears very similar in the two instruments, although the observations are not simultaneous.

Since the values of the parameters obtained by fitting the *XMM-Newton* and *BeppoSAX* spectra in the soft state are very similar, we fitted these data simultaneously, adding the RXTE data. The different cross calibrations of the different instruments were taken into account by including normalizing factors in the model. This factor was fixed to 1 for pn and kept free for the

Table 2. Parameters left free to vary between *XMM-Newton*, *BeppoSAX*, and RXTE spectra in the soft state.
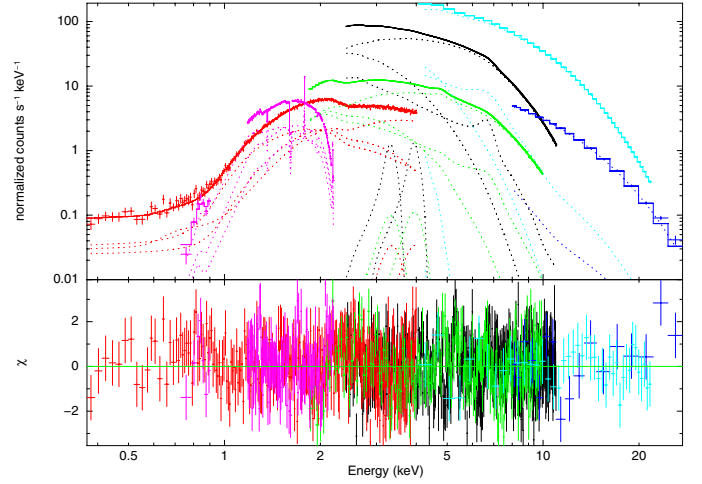
Parameter	XMM	BeppoSAX	RXTE
N_H ($\times 10^{22}$ cm^{-2})	2.08 ± 0.02	1.96 ± 0.02	3.64 ± 0.02
Γ	2.6 ± 0.1	2.2 ± 0.1	2.4 ± 0.1
kT_e (keV)	3.0 ± 0.1	2.9 ± 0.1	B
kT_{seed} (keV)	1.30 ± 0.02	$1.13^{+0.01}_{-0.02}$	B
$Norm_{nthComp}$	0.14 ± 0.01	0.19 ± 0.01	B

Notes. The whole model is presented in Table 7. B: corresponding parameter has the same value as in the *BeppoSAX* spectrum.

Fig. 6. *Top panel*: XMM/RGS1 (magenta), XMM/EPIC-pn (black), *BeppoSAX*/LECS (red), *BeppoSAX*/MECS (green), *BeppoSAX*/HPGSPC (blue), RXTE/PCA (cyan) data points in the range 0.3–30 keV, when 4U 1705−44 was in the soft state. *Bottom panel*: residuals (data-model) in unit of σ when the REFLIONX model is used to describe the reflection component. The parameters associated to this model are indicated in Table 7. The XMM/RGS1 data have been rebinned for graphical purpose.

other instruments. We used the self-consistent reflection model REFLIONX, and NTHCOMP instead of COMPTT, to describe the thermal Comptonization component in order to have the photon index as a parameter of the fit. To take the disk smearing into account, which is necessary to obtain a good fit of the reflection component, we convolved the reflection model, the edge, and the two Gaussians used to fit the Ar and Ca lines with the same RDBLUR component.

Since the spectra are not simultaneous, we find small differences in the best fit values of some parameters of the continuum model. We therefore left these parameters free to vary from one instrument to the next, when necessary (see Table 2). These parameters are the column density, the parameters of NTHCOMP (the photon index, the temperature of the electrons and of the seed photons, and the normalization) and the fold energy of the high-energy cutoff (that is fixed at 2.7 times the electron temperature in the soft state, according to the expectation for saturated Comptonization), which are slightly different for *BeppoSAX* and *XMM-Newton*. As regards RXTE, only the column density and the photon index are left free to vary. The other parameters coincide very well with those found for the *BeppoSAX* spectrum, so they are constrained to have the same values. All the other parameters are perfectly consistent with those obtained for *XMM-Newton*, and were forced to have the same values. The total χ^2/d.o.f. obtained in this way is 1839/1573 ($\chi^2_{red} \sim 1.17$).

We note that the RDBLUR component is not statistically required to fit the whole dataset in this case. Indeed, if we delete this component from the model, we obtain χ^2 = 1835/1574 (~ 1.17), which is very similar to the one we get when the relativistic smearing is included in the model (χ^2/d.o.f. = 1839/1573). However, if we exclude the relativistic smearing from the model, the ionization parameter gets an extremely high value, ~ 8000 erg cm s^{-1}, that appears to be unphysical. At such a high ionization parameter, Fe XXVI would be the most abundant Fe ion and this would produce a line at 6.97 keV. On the other hand, in the *XMM-Newton* spectrum the iron line is clearly detected at 6.7 keV, suggesting it is produced by Fe XXV. With the inclusion of the relativistic smearing described by the RDBLUR component, the ionization parameter attains a more reasonable value of 3500, fully consistent with the presence of an iron line at 6.6 keV produced by Fe XXV. Moreover, all the smearing parameters are perfectly coherent with those previously obtained (e.g. Di Salvo et al. 2009; D'Aì et al. 2010; Piraino et al. 2007). An additional iron edge is found at 8.7 keV with a significance of 11.6 σ. Finally, we report here, for the first time, evidence of an iron overabundance by a factor 2.5 with respect to its solar abundances. The results of this model are presented in Table 7. To evaluate the statistical significance of the iron overabundance,

we fixed this parameter to one. The χ^2 increases by 48 for the addition of 1 d.o.f. ($\chi^2_{red} \sim 1.20$) and the associated probability of chance improvement is 2×10^{-10}, so the iron overabundance is statistically significant.

The EPIC/pn absorbed flux obtained from the *XMM-Newton* best fit spectral parameters is 6.19×10^{-9} erg cm^{-2} s^{-1} and the unabsorbed flux is 7.39×10^{-9} erg cm^{-2} s^{-1} in the 2−10 keV band. We extrapolate this model in the 0.1−150 keV range to estimate the bolometric unabsorbed flux, $F_X = 2.7(1) \times 10^{-8}$ erg cm^{-2} s^{-1}. The bolometric luminosity associated to the soft state is $L_X \sim 1.8 \times 10^{38}$ erg s^{-1}, assuming a distance to the source of 7.4 kpc. This value is very close to the Eddington luminosity for a 1.4 $M_\odot$ neutron star.

We also apply another reflection model, XILLVER (Garcia & Kallman 2010), to our dataset of 4U 1705−44 from the three satellites. This model includes Compton broadening, and the illumination spectrum is a power law with a photon index of two, similar to REFLIONX. In this model, the redistribution of the photon energy is achieved by a Gaussian convolution, whose sigma is a function of the energy and the temperature of the gas. The gas temperature changes when going deep inside the disk, and is calculated self-consistently by solving thermal and ionization balance. This model also includes emission lines from the same ions included in REFLIONX and, in addition, emission lines from Ar and Ca. It also allows fitting the abundances of these two elements with respect to the solar abundance. In this case, to obtain a stable fit, we were forced to freeze the photon index Γ associated to the *XMM-Newton* data to the value obtained with REFLIONX ($\Gamma = 2.6$). The addition of the edge at 8.5 keV is again needed to improve the fit, with a significance of 11.1σ. The χ^2_{red} associated to this fit is 1.26 for 1576 d.o.f. The fit obtained with this model is a bit worse than obtained with REFLIONX, but the values of the parameters are still consistent with those obtained with REFLIONX. We note a lower value of the inclination angle of the system ($i = 25-27°$), while the value of the inner disk radius ($R_{in} = 10-13 \, R_g$) is perfectly consistent between
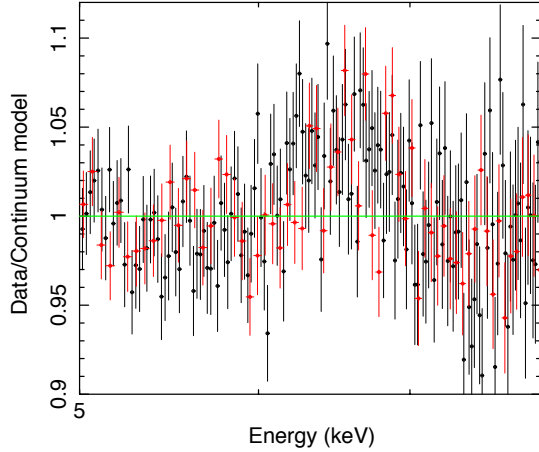
Fig. 7. Ratio of the data to the best-fit continuum model for XMM/EPIC-pn (black) and *BeppoSAX*/MECS (red) in the hard state, in the energy range 5−8 keV. The broad iron line is visible in both spectra, but is not as well defined as in the soft state (see Fig. 5). The continuum is described by phabs (bbody + compTT).

Table 3. Parameters left free to vary between *XMM-Newton*, *BeppoSAX*, and RXTE in the hard state.

| Parameter	XMM	BeppoSAX	RXTE
N_H ($\times 10^{22}$ cm^{-2})	2.0 ± 0.3	1.9 ± 0.1	B
kT_{bb} (keV)	$0.58^{+0.04}_{-0.02}$	$0.24^{+0.02}_{-0.03}$	B
$Norm_{bb}$ ($\times 10^{-3}$)	2.6 ± 0.5	2.0 ± 0.4	B
Γ	B	1.84 ± 0.01	$2.07^{+0.05}_{-0.03}$
kT_e (keV)	B	22^{+2}_{-1}	79^{+50}_{-22}

Notes. The complete model is given in Table 8. B: corresponding parameter is fixed to have the same value as in the *BeppoSAX* spectrum. kT_{bb}, $Norm_{bb}$: temperature and normalization of the BLACKBODY component. Γ, kT_e: photon index and electron temperature of the NTHCOMP component.

the two cases[4]. We find an overabundance by a factor 1.5−2 of Ar and Ca with respect to their solar abundance; a similar overabundance is also observed for iron (see Table 7). However, the statistical significance of the overabundance of Ar and Ca is not very well established. Indeed, fixing this parameter to 1, we find χ^2/d.o.f. = 1992/1577, the corresponding probability of chance impovement is 2×10^{-2}. In any case, this model allows us to demonstrate that the Ar and Ca lines are probably produced by reflection.

As seen in the previous section, PEXRIV also gives a very good fit of the pn data. We apply this model plus four Gaussians, all convolved with the same rdblur component, to the whole dataset. The results are very similar to REFLIONX, in particular the inclination of the system ($i = 38-41°$) and the inner radius of the accretion disk ($R_{in} = 12-17 R_g$). The χ^2_{red} associated is 1.16 for 1570 d.o.f. The best fit parameters corresponding to this model are summarized in Table 7 and compared to REFLIONX and XILLVER.

5. Hard state

In this section we apply the same procedure used for the soft state to the 4U 1705−44 data in the hard state, using the three satellites: *XMM-Newton*, *BeppoSAX*, and RXTE. Regarding the *XMM-Newton* data, we excluded a type-I X-ray burst before performing the spectral analysis. The study of the burst is described by D'Aì et al. (2010).

We use the same continuum model in order to determine the differences in the spectral parameters from one state to the other. The temperature of the electrons is about 14−16 keV, the temperature of the seed photons is 1.0−1.2 keV, the optical depth of the Comptonized component is 5−6, and the blackbody is

found at 0.55−0.58 keV. The addition of a Gaussian improves considerably the fit. A broad iron line is present in all the data at 6.4−6.6 keV (see Fig. 7). Using a DISKLINE instead of a Gaussian profile to fit the iron line, we have to freeze the values of the outer radius to 3500 R_g and the inclination of the system to 37°, as in the soft state and in agreement with Di Salvo et al. (2009). The χ^2 in this case is the same as using a simple Gaussian line. While for the *XMM-Newton* data, the χ^2/d.o.f. is 407/419 ($\sim$0.97) using a Gaussian, there are still some residuals at high energy (>10 keV) in the case of *BeppoSAX* and RXTE. The associated χ^2_{red} are 1.24 (484 d.o.f.) and 1.15 (65 d.o.f.) for the *BeppoSAX* and the RXTE spectra, respectively.

To fit this hard excess, probably ascribed to the Compton bump of the reflection component, we apply the self-consistent reflection model REFLIONX, with the aim of comparing the values of the parameters in the hard state and in the soft state. In this case we fix the folding energy of the high-energy cutoff to the electron temperature of the NTHCOMP component, as expected for unsaturated Comptonization. We simultaneously fitted the three datasets following the same method as described in previous section. Some parameters are left free to vary between the instruments of the different observatories, such as the column density and the blackbody temperature. Moreover, in the case of the RXTE spectrum, we have to leave the photon index of the power law and the electron temperature free to vary in order to obtain a good fit. These parameters are listed in Table 3. The inclination angle is not well constrained so we freeze its value to 37°, which corresponds to the best fit value obtained in the soft state using REFLIONX to fit the reflection component. The outer radius of the accretion disk is also frozen to 3500 R_g. This value corresponds to the best estimate obtained using the REFLIONX model to fit the soft state of 4U 1705−44 and is consistent with the results reported by Di Salvo et al. (2009).

We convolve the reflection model with the RDBLUR component to include Doppler broadening caused by the motion of matter in the inner disk. The addition of this component decreases the χ^2/d.o.f. from 1126/981 to 1097/980. The F-test is $\sim 4 \times 10^{-7}$. This demonstrates that the iron line and the whole reflection component are also significantly broadened in the hard state, and are consistent with being produced in the accretion disk. Since only the iron line is significantly detected, we do not add any other emission line or edge. To measure the significance of the Compton bump in these data, we replace the REFLIONX model with a simple Gaussian line smeared by relativistic and/or Doppler effects, by using the RDBLUR component. The χ^2 is 1299/981 $\sim$1.32. We compare this result with the previous

---

[4] We use here a test version of the XILLVER model, specifically developed to include Ar and Ca lines. In this version of the model, the illuminating flux is integrated over a different energy range with respect to that used for the REFLIONX model, and this results in a different, lower value of the ionization parameter, which also affects the estimate of the inclination angle (Garcia, priv. comm.). We have checked that, integrating the illumination flux over the same range used for the REFLIONX model, we obtain best-fit parameters that are all compatible with those obtained with REFLIONX.
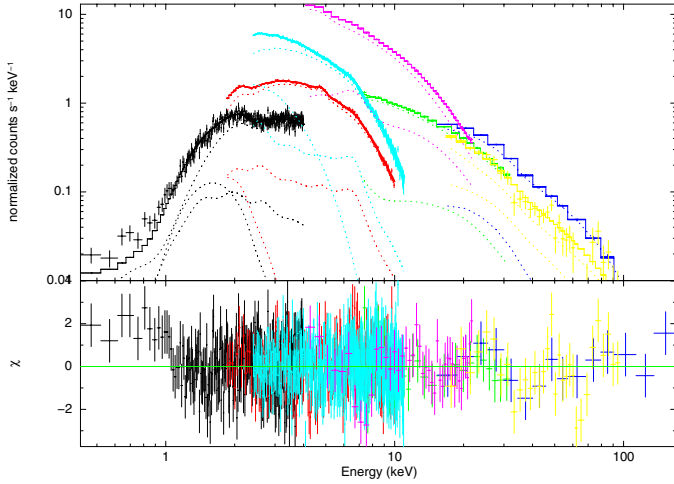
Fig. 8. *Top panel*: XMM/EPIC-pn (cyan), *BeppoSAX*/LECS (black), *BeppoSAX*/MECS (red), *BeppoSAX*/HPGSPC (green), *BeppoSAX*/PDS (blue), RXTE/PCA (magenta), RXTE/HXTE (yellow) data points in the range 0.4–200 keV, corresponding to the hard state of 4U 1705−44. *Bottom panel*: residuals (data-model) in units of σ when the REFLIONX model is applied. The parameters associated to this model are shown in Table 8.

model where the reflection component is included instead of the simple Gaussian associated to the iron line. The F-test gives a probability of chance improvement equal to 10^{-38}. This shows that there is a reflection signature in the spectrum besides the iron line in the hard state, meaning the Compton bump is significantly detected in these data.

We obtain a good fit of the whole dataset; the best fit parameters are listed in Table 8, where we just show those obtained for the *BeppoSAX* spectrum. (There are small differences in the best-fit parameters related to the fact that the observations are not simultaneous as described above.) From all the instruments, we obtain a constraint on the inner disk radius, which appears to be truncated farther from the neutron star surface ($R_{in} = 19$–$59\,R_g$) with respect to the soft state. We obtain a high temperature of the electrons (about 22 keV) in the hard state, and a low value of the ionization parameter ($\xi \sim 210$ erg cm s^{-1}).

The absorbed flux associated to this model obtained from the *BeppoSAX* best fit parameters in the range 0.1–150 keV is 2.09×10^{-9} erg cm^{-2} s^{-1}, and the unabsorbed flux is 2.99×10^{-9} erg cm^{-2} s^{-1}. The bolometric luminosity associated to the hard state is $L_X \sim 2 \times 10^{37} d_{7.4}^2$ erg s^{-1}, which corresponds to $\sim 11\%\ L_{Edd}$.

Because in the soft state, an iron overabundance has been detected by at least a factor 2, we fixed this parameter to two in order to evaluate the change in the whole spectrum and its effect on the other parameters. The values of the parameters are very similar, even if the χ^2 is a bit higher (1.13 for 981 d.o.f.). The inner disk radius is found at a slightly larger distance from the compact object ($R_{in} = 24$–$79\,R_g$), again in agreement with a geometry where the accretion disk is truncated farther from the neutron star than in the soft state. These results are summarized in Table 8.

6. Discussion

We performed a spectral analysis in the broad band and with high energy resolution of 4U 1705−44 using data from *XMM-Newton*, *BeppoSAX*, and RXTE, both in the hard and in the soft state. We described a method of fitting unsimultaneous

data, which we applied using self-consistent reflection models. Thanks to the good spectral coverage from the low (0.3 keV) to the high (200 keV) energy band, we have obtained good constraints on the continuum emission and on the reflection component, marking the most significant changes in the spectral parameters from the hard state to the soft state. The agreement between the results obtained with different instruments and the possibility of fitting most of the reflection component with self-consistent models, provides further evidence that the broad iron line observed in 4U 1705−44 may be produced by reflection at the inner accretion disk, and indicates that the reported inner disk parameters are indeed reliable. In the following we discuss the main results from this analysis.

6.1. The iron line

The origin of the iron line in neutron star LMXBs is still being debated (Ng et al. 2010; Cackett et al. 2010, 2012). In this paper, we have compared the iron line profile observed by *XMM-Newton* with the one observed by other instruments, and in particular by *BeppoSAX*. We find perfect agreement between the results from these instruments, although the observations were not simultaneous, both in the soft and in the hard state of the source.

We carefully studied the pile-up effects in the XMM/EPIC-pn spectrum of 4U 1705−44 during the soft state, when the count rate was the highest. We demonstrated that the exclusion of the two central columns of the CCD is enough to get rid of pile-up effects, while excluding more CCD rows may underestimate the number of double events with respect to the expected value (see Appendix). In addition to this, we showed that the addition of the RGS data is important to constrain the overall continuum shape well. We find that the iron line parameters are not significantly affected by pile-up. This agrees with Cackett et al. (2010), who also conclude that the iron line profile is robust even if there was a small fraction of pile-up affecting the data, while the continuum may vary significantly. This also agrees with a comprehensive study performed by Miller et al. (2010), who found that severe pile-up may distort disk lines and the continuum shape, whereas a modest pile-up fraction does not noticeably affect the line shape. This is probably the case of 4U 1705−44. The best fit parameters of the iron line profile we find in this way agree perfectly with what has been previously found (see e.g. Piraino et al. 2007; Di Salvo et al. 2009; D'Aì et al. 2010), independently of the particular model used to fit the reflection component.

In the soft state, the Fe line at 6.7 keV is associated with highly ionized Fe XXV, which is a triplet consisting of the following components: at $r = 6.700$ keV, $i_2 = 6.682$ keV, $i_1 = 6.668$ keV, and $f = 6.637$ keV. We also included a Gaussian to consider the H-like Fe XXVI contribution of the Lyα transitions at $Ly\alpha_1 = 6.973$ keV and $Ly\alpha_2 = 6.952$ keV. Unfortunately, the resolution of *XMM-Newton* and *BeppoSAX* does not allow us to resolve the structure of the resulting line, which appears to be dominated by the intercombination line of the triplet, and this is why a single Gaussian or a diskline has been used to take all these components into account. These lines were resolved, for example, in the case of the bright Z-source Cyg X-2 observed with the High Energy Transmission Grating Spectrometer on-board the *Chandra* satellite, which offers very high spectral resolution (Schulz et al. 2009). Also in that case the Fe complex was dominated by the intercombination line of the Fe XXV triplet, and therefore the line was fitted by a single Gaussian. Also a red-skewed wing of the iron line was discovered in a *Suzaku* observation of Cyg X-2 (Shaposhnikov et al. 2009). It should be noted,

Table 4. *XMM-Newton* and *BeppoSAX* journal of observations.

Satellite	Obs. ID	Obs. date	Exp. time (ks)	Count rate ASM (c/s)	State source
XMM-Newton	0402300201	26/08/2006	34.72	1	Hard
	0551270201	24/08/2008	45.17	19	Soft
BeppoSAX	21292001	20/08/2000	43.5	18	Soft
		03/10/2000	48	3	Hard

Table 5. Selected RXTE observation journal.

Source state	Obs. ID	Obs. date (MJD)	Count rate (c/s)	Hardness
SS	93060-01-15-00	54 332.3	642.4	0.613
	93060-01-16-00	54 336.4	804.4	0.647
	93060-01-19-01	54 348.7	1049.0	0.620
	93060-01-19-02	54 349.0	1011.0	0.621
	93060-01-25-00	54 372.5	834.5	0.630
	93060-01-76-00	54 576.5	726.9	0.620
	93060-01-84-00	54 608.5	833.7	0.628
	93060-01-91-00	54 636.8	732.4	0.625
	93060-01-95-00	54 652.6	785.0	0.617
	93060-01-01-10	54 668.1	832.2	0.646
	93060-01-02-10	54 672.3	849.8	0.637
	93060-01-07-10	54 692.5	761.5	0.614
	93060-01-10-10	54 704.4	768.4	0.632
	93060-01-12-10	54 712.2	791.4	0.617
	93060-01-19-10	54 740.3	782.5	0.631
	94060-01-20-00	54 942.5	805.5	0.609
	94060-01-22-00	54 950.6	834.7	0.622
	95060-01-71-00	55 478.6	879.0	0.620
HS	91039-01-01-41	53 541.0	79.7	0.760
	91039-01-01-42	53 543.0	78.1	0.749
	91039-01-01-43	53 544.8	82.6	0.751
	91039-01-01-50	53 546.0	91.3	0.767
	91039-01-02-40	53 658.3	64.9	0.736
	93060-01-07-00	54 300.4	70.6	0.747
	93060-01-52-01	54 480.6	67.1	0.746
	94060-01-08-00	54 894.9	52.1	0.738
	95060-01-19-01	55 270.5	69.6	0.749
	95060-01-33-00	55 326.4	52.5	0.733
	95060-01-46-00	55 378.7	57.7	0.750

however, that these lines are all included in the reflection models we used in our spectral analysis, and a further smearing was required to properly fit the line complex. Consequently, the iron line is consistent with being produced in the inner part of the accretion disk where the line profile is distorted by Doppler and by mildly relativistic effects relatively close to the compact object. At the inner disk radii we find, $R_{in} \sim 10-17 R_g$, the Keplerian velocities become mildly relativistic, and the Doppler boosting effect yields the blue-shifted horn (produced by matter coming in our direction) brighter than the red-shifted one (produced by receding matter).

In the hard state, the Fe emission line at 6.4−6.6 keV is related to a low ionized Fe fluorescence line. The line does not present clear asymmetry anymore and is equally well fit by a Gaussian or with the diskline model. The apparent symmetry of the line may be due to the relativistic effects becoming less important farther from the compact object and/or to the lower statistics in the hard state. In both states, the broadening of the line is not as extreme as in the case of some black hole X-ray binaries or AGNs (see e.g. Reis et al. 2009a; Fabian et al. 2009). The Compton hump of the reflection component, however, is required with a very high confidence level to get a good fit of the data in the hard state.

6.2. Reflection models

We used data of 4U 1705−44 from three satellites (*XMM-Newton*, *BeppoSAX*, and RXTE) in order to test self-consistent reflection models on a broad-band range from 0.3 to 200 keV. The reflection models we used are calculated for an optically-thick atmosphere (such as the surface of an accretion disk) of constant density illuminated by a power-law spectrum.

In the soft state, we conclude that the reflection model PEXRIV is able to fit the iron edge with smearing parameters that are very similar to those obtained for the iron line profile; the REFLIONX model is able to self-consistently fit the iron line profile and the S XVI line at 2.6 keV; the XILLVER model is able to fit the iron line profile self-consistently with the S XVI, the Ar XVII, and Ca XIX lines. The REFLIONX model suggests an iron overabundance by a factor of about 2 with respect to its solar abundance. A mildly relativistic smearing of the reflection component, described with the RDBLUR component, is statistically required to fit the *XMM-Newton* data with the REFLIONX model, because these data have the best statistics at the iron line energy. Nevertheless, this component is not statistically required when we fit all our dataset with the REFLIONX model. However, if we exclude the RDBLUR component from the model,

Table 6. Evaluation of the pile-up effects on the *XMM-Newton* EPIC-pn data of 4U 1705−44 in the soft state, using the RGS and pn spectra.

Component	Parameter	pn-all	pn-1	pn-2	pn-3	pn-4	pn-5	pn-6	pn-7	BeppoSAX
phabs	$N_{\rm H}$ (×10^{22} cm^{-2})	1.6 ± 0.1	1.6 ± 0.1	1.6 ± 0.1	1.6 ± 0.1	1.6 ± 0.1	1.6 ± 0.1	1.6 ± 0.1	1.6 ± 0.1	1.9 ± 0.1
rdblur	Betor	$-2.30^{+0.04}_{-0.02}$	-2.32 ± 0.03	$-2.35^{+0.05}_{-0.04}$	$-2.39^{+0.06}_{-0.07}$	$-2.35^{+0.04}_{-0.07}$	$-2.39^{+0.08}_{-0.07}$	-2.4 ± 0.1	-2.4 ± 0.1	−2 (frozen)
rdblur	$R_{\rm in}$ (GM/c^2)	14 ± 2	14^{+1}_{-2}	14^{+3}_{-1}	15 ± 2	15^{+3}_{-2}	16 ± 3	16^{+4}_{-3}	17^{+4}_{-3}	8^{+4}_{-2}
rdblur	i (°)	38 ± 1	39 ± 1	38^{+2}_{-1}	39 ± 2	41^{+2}_{-1}	42 ± 2	40^{+3}_{-2}	40^{+6}_{-3}	28^{+20}_{-8}
edge	E (keV)	8.6 ± 0.1	8.6 ± 0.1	8.6 ± 0.1	8.6 ± 0.1	8.7 ± 0.1	$8.7^{+0.2}_{-0.1}$	8.8 ± 0.2	$8.6^{+0.3}_{-0.5}$	–
edge	Max τ (×10^{-2})	5.1 ± 0.4	5.7 ± 0.4	7 ± 1	7 ± 1	8 ± 2	8 ± 2	7^{+3}_{-2}	5^{+3}_{-2}	–
bbody	$kT_{\rm bb}$ (keV)	0.57 ± 0.01	0.57 ± 0.01	0.57 ± 0.01	0.56 ± 0.01	0.55 ± 0.02	0.55 ± 0.02	0.54 ± 0.01	0.54 ± 0.02	0.56 ± 0.01
bbody	Norm (×10^{-2})	3.0 ± 0.1	2.9 ± 0.1	3.1 ± 0.1	3.0 ± 0.1	3.2 ± 0.1	3.2 ± 0.1	3.4 ± 0.1	3.4 ± 0.1	2.2 ± 0.1
compTT	$kT_{\rm o}$ (keV)	1.31 ± 0.01	1.29 ± 0.02	$1.30^{+0.02}_{-0.03}$	$1.34^{+0.02}_{-0.05}$	$1.33^{+0.03}_{-0.08}$	$1.35^{+0.05}_{-0.09}$	1.36 ± 0.05	$1.39^{+0.06}_{-0.04}$	$1.13^{+0.05}_{-0.02}$
compTT	$kT_{\rm e}$ (keV)	6^{+19}_{-2}	4^{+3}_{-1}	4^{+4}_{-1}	4^{+14}_{-1}	4^{+11}_{-1}	4^{+15}_{-2}	4^{+18}_{-1}	4^{+5}_{-1}	2.7 ± 0.1
compTT	τ	$4.7^{+13}_{-0.1}$	6.8 ± 0.1	$6.6^{+0.1}_{-0.3}$	5.9 ± 0.3	6^{+7}_{-1}	$5.2^{+0.6}_{-0.5}$	$5.1^{+0.5}_{-0.6}$	4^{+60}_{-1}	11.0 ± 0.6
compTT	Norm (×10^{-2})	18^{+6}_{-5}	29^{+8}_{-2}	30 ± 1	30^{+65}_{-2}	30^{+1}_{-7}	30^{+1}_{-12}	33^{+170}_{-12}	32^{+411}_{-8}	35 ± 2
gauss	E (keV)	2.64 ± 0.03	2.67 ± 0.03	2.65 ± 0.03	2.65 ± 0.03	2.67 ± 0.05	2.66 ± 0.05	$2.7^{+0.9}_{-0.7}$	$2.8^{+0.1}_{-0.2}$	–
gauss	Norm (×10^{-3})	0.9 ± 0.2	1.3 ± 0.2	2.1 ± 0.3	$1.6^{+0.5}_{-0.3}$	1.7 ± 0.6	$1.8^{+0.8}_{-0.7}$	$1.8^{+0.8}_{-0.9}$	$1.3^{+0.9}_{-0.7}$	–
gauss	E (keV)	3.29 ± 0.01	$3.29^{+0.01}_{-0.02}$	3.29 ± 0.02	$3.30^{+0.03}_{-0.02}$	$3.30^{+0.03}_{-0.02}$	$3.27^{+0.04}_{-0.02}$	3.27 ± 0.03	$3.28^{+0.03}_{-0.04}$	–
gauss	Norm (×10^{-3})	1.9 ± 0.2	2.1 ± 0.2	2.4 ± 0.2	2.6 ± 0.3	$3.2^{+0.3}_{-0.5}$	3.1 ± 0.6	$3.4^{+0.5}_{-0.7}$	2.8 ± 0.7	–
gauss	E (keV)	$3.89^{+0.01}_{-0.02}$	$3.87^{+0.04}_{-0.01}$	3.89 ± 0.02	3.88 ± 0.02	3.88 ± 0.02	3.86 ± 0.03	$3.84^{+0.03}_{-0.02}$	$3.87^{+0.03}_{-0.05}$	–
gauss	Norm (×10^{-3})	1.7 ± 0.1	2.0 ± 0.1	2.1 ± 0.2	2.4 ± 0.2	2.9 ± 0.4	$3.0^{+0.5}_{-0.2}$	3.3 ± 0.6	$3.1^{+0.9}_{-0.6}$	–
gauss	E (keV)	6.64 ± 0.01	6.64 ± 0.01	6.64 ± 0.01	6.62 ± 0.02	$6.62^{+0.03}_{-0.02}$	$6.59^{+0.02}_{-0.03}$	6.58 ± 0.04	6.58 ± 0.04	$6.7^{+0.2}_{-0.5}$
gauss	Norm (×10^{-3})	$3.8^{+0.1}_{-0.2}$	4.1 ± 0.2	4.3 ± 0.1	$4.1^{+0.3}_{-0.2}$	4.4 ± 0.4	4.7 ± 0.4	$4.9^{+0.5}_{-0.4}$	$4.6^{+0.6}_{-0.4}$	$4.7^{+2}_{-0.6}$
	$\chi^2_{\rm red}$ (d.o.f.)	1.20 (1024)	1.15 (1024)	1.14 (1024)	1.15 (1024)	1.13 (1024)	1.11 (1024)	1.13 (1024)	1.14 (1024)	1.18 (524)

Notes. We compare the parameters obtained when we exclude 0, 1, 2, until the 7 brightest central columns in the pn CCD, which correspond to spectra named pn-all, pn-1, pn-2, up to pn-7, respectively (see text). The last column contains the results from *BeppoSAX* data in the soft state as reported by Piraino et al. (2007), to compare the values of the parameters obtained with *XMM-Newton* with those obtained with non-CCD instruments. The model applied on the pn and RGS data consists of const*phabs*rdblur*edge*(bbody+compTT+gauss+gauss+gauss+gauss). The model used to fit the *BeppoSAX* data is phabs*(bbody+compTT+powerlaw+diskline).

Table 7. Comparison of three different self-consistent, relativistically smeared reflection models (reflionx, xillver and pexriv) applied to the *XMM-Newton*, *BeppoSAX*, and RXTE spectra of 4U 1705−44 in the soft state.

Component	Parameter	Reflionx	Xillver	Pexriv
phabs	N_H ($\times 10^{22}$ cm^{-2})	2.08 ± 0.02	2.04 ± 0.01	1.91 ± 0.02
bbody	kT_{bb} (keV)	0.56 ± 0.01	$0.67^{+0.02}_{-0.01}$	0.52 ± 0.01
bbody	Norm ($\times 10^{-2}$)	2.58 ± 0.01	1.7 ± 0.01	2.94 ± 0.01
nthComp	Γ	2.6 ± 0.1	2.6 (frozen)	2.3 ± 0.1
nthComp	kT_e (keV)	3.0 ± 0.1	2.9 ± 0.1	2.6 ± 0.1
nthComp	kT_{seed} (keV)	1.30 ± 0.02	$1.39^{+0.04}_{-0.01}$	$1.18^{+0.03}_{-0.02}$
nthComp	Norm	0.14 ± 0.01	0.11 ± 0.01	0.17 ± 0.01
rdblur	Betor	-2.1 ± 0.1	-2.1 ± 0.1	-2.3 ± 0.1
rdblur	R_{in} (GM/c^2)	13 ± 3	11^{+2}_{-1}	15^{+2}_{-3}
rdblur	R_{out} (GM/c^2)	3500 (frozen)	3500 (frozen)	3500 (frozen)
rdblur	i (°)	37 ± 2	26 ± 1	40^{+1}_{-2}
edge	E (keV)	8.7 ± 0.1	8.5 ± 0.1	–
edge	Max τ ($\times 10^{-2}$)	4.2 ± 0.6	3.4 ± 0.5	–
gauss	E (keV)	–	–	2.6 (frozen)
gauss	Norm ($\times 10^{-3}$)	–	–	1.4 ± 0.2
gauss	E (keV)	3.31 ± 0.01	–	$3.31^{+0.02}_{-0.03}$
gauss	Norm ($\times 10^{-3}$)	1.4 ± 0.2	–	1.9 ± 0.2
gauss	E (keV)	3.92 ± 0.02	–	$3.88^{+0.01}_{-0.03}$
gauss	Norm ($\times 10^{-3}$)	1.4 ± 0.2	–	2.0 ± 0.2
gauss	E (keV)	–	–	6.63 ± 0.01
gauss	Norm ($\times 10^{-3}$)	–	–	4.1 ± 0.1
highecut	cutoff$_E$ (keV)	0.1 (frozen)	0.1 (frozen)	–
highecut	fold$_E$ (keV)	8.1 (2.7*kT$_e$ of nthComp)	7.7 (2.7*kT$_e$ of nthComp)	7.0 (2.7*kT$_e$ of nthComp)
reflection	Γ	2.6 (=Γ of nthComp)	–	2.3 (=Γ of nthComp)
reflection	Norm	$(8 \pm 1) \times 10^{-6}$	$(1.5 \pm 0.1) \times 10^{-5}$	1.218 (frozen)
reflection	Fe/Solar	$2.5^{+0.4}_{-0.5}$	1 (frozen)	$1.4^{+0.6}_{-0.1}$
reflection	Ar, Ca Abund	1 (frozen)	$1.8^{+0.2}_{-0.3}$	1 (frozen)
reflection	ξ (erg cm s^{-1})	3578^{+1184}_{-847}	1349^{+31}_{-90}	3081^{+2488}_{-1954}
pexriv	Rel-refl	–	–	$-1^{+1}_{-0.02}$
	Total χ^2_{red} (d.o.f.)	1.17 (1573)	1.26 (1576)	1.16 (1570)

Notes. The model used is const*phabs*rdblur*edge*(bbody+nthcomp+gauss+gauss+ gauss+gauss+highecut*reflection). For the pexriv model, the disk inclination is fixed to cos i = 0.78 and the disk temperature to 10^6 K. Here we present the best fit parameters we obtain for the *XMM-Newton* spectrum. A few parameters of the continuum got different best fit values for the nonsimultaneous *BeppoSAX* and RXTE spectra, as detailed in Table 2.

we find that the ionization attains very high (unphysical) values. It should be noted here that both REFLIONX and XILLVER include Compton broadening, which is higher for higher ionization parameters (Reis et al. 2009b). This means that to adequately fit the width of the line with Compton broadening alone, we have to dramatically increase the ionization parameter to values that appear too high to be compatible with the observed energy of the iron line. This is why we decided to include the relativistic smearing in the reflection model. The smearing parameters are determined well and appear very similar regardless of the particular reflection model adopted. They are congruent with previous results reported for this source (Piraino et al. 2007; Di Salvo et al. 2009; D'Aì et al. 2010), and are very similar for all the datasets used here (from *XMM-Newton*, *BeppoSAX*, and RXTE satellites).

In the hard state, we significantly detect the iron line at 6.4 keV and the Compton bump of the reflection component, while the other low-energy emission lines and the iron edge were not significantly detected. We just used the REFLIONX model to fit the reflection component self-consistently (i.e. just the iron line and the Compton bump in this case). As before, we obtain a very good fit of the whole spectrum in the broad-energy band between 0.4 and 200 keV. We note that the relativistic smearing

is statistically required for the hard state. In fact the iron line is found to also be broad in this state (although not as broad as in the soft state), but in that case the ionization parameter has a particularly low value, and Compton broadening is negligible so cannot explain the width of the line. Our results for the hard state of 4U 1705-44 coincide with the results obtained by Piraino et al. (in preparation). These authors fit the *BeppoSAX* data in the hard state with an alternative reflection model, where COMPPS (Poutanen & Svensson 1996) is used to model the primary Comptonization spectrum. Their results are consistent with the disk-reflection scenario we favor in this paper.

Our results agree with Reis et al. (2009b), who applied RE-FLIONX on three datasets of 4U 1705−44 obtained by *Suzaku* at different periods. A relativistic broadening was also required to obtain a good fit, as in our analysis. Therefore different instruments get similar values for the reflection component in 4U 1705−44, indicating that the iron line shape as seen by these instruments is similar, and demonstrating that pile-up is not responsible for the observed iron line shape.

D'Aì et al. (2010) and Cackett et al. (2010) also applied a reflection model, REFBB (Ballantyne 2004), to fit the spectrum of this source, restricted to the *XMM-Newton* data in the energy range 2–12 keV. In this model a blackbody component, very

Table 8. Self-consistent, relativistically smeared reflection model (reflionx) applied to the 4U 1705−44 spectra from the three satellites (*XMM-Newton*, *BeppoSAX*, and RXTE) when the source was in the hard state.

Component	Parameter	Reflionx (Fe/sol = free)	Reflionx (Fe/sol = 2)
phabs	N_H ($\times 10^{22}$ cm^{-2})	1.9 ± 0.1	1.9 ± 0.1
bbody	kT_{bb} (keV)	$0.24^{+0.02}_{-0.03}$	0.26 ± 0.02
bbody	Norm ($\times 10^{-3}$)	2.0 ± 0.4	1.7 ± 0.3
nthComp	Γ	1.84 ± 0.01	1.83 ± 0.01
nthComp	kT_e (keV)	22^{+2}_{-1}	21 ± 1
nthComp	kT_{seed} (keV)	$0.69^{+0.02}_{-0.01}$	0.70 ± 0.02
nthComp	Norm ($\times 10^{-2}$)	$3.9^{+0.1}_{-0.2}$	4.0 ± 0.2
rdblur	Betor	-3 (frozen)	-3 (frozen)
rdblur	R_{in} (GM/c^2)	31^{+28}_{-12}	39^{+40}_{-15}
rdblur	R_{out} (GM/c^2)	3500 (frozen)	3500 (frozen)
rdblur	i (°)	37 (frozen)	37 (frozen)
highecut	$cutoff_E$ (keV)	0.1 (frozen)	0.1 (frozen)
highecut	$fold_E$ (keV)	22 (=kT_e of nthComp)	21 (=kT_e of nthComp)
reflionx	Fe/Solar	$1.1^{+0.5}_{-0.3}$	2 (frozen)
reflionx	Γ	1.84 (=Γ of nthComp)	1.83 (=Γ of nthComp)
reflionx	ξ (erg cm s^{-1})	209^{+9}_{-5}	204^{+4}_{-3}
reflionx	Norm ($\times 10^{-5}$)	1.7 ± 0.3	$1.8^{+0.6}_{-0.3}$
	Total χ^2_{red} (d.o.f.)	1.12 (980)	1.13 (981)

Notes. The model consists of const*phabs*(bbody + nthComp + rdblur*highecut*reflionx). The inclination angle is fixed at 37°, while the Fe/sol ratio is left free to vary or is fixed to 2. Here we show the best fit parameters we obtain for the *BeppoSAX* spectrum. A few parameters of the continuum got different best fit values for the nonsimultaneous *XMM-Newton* and RXTE spectra, as detailed in Table 3.

likely associated to the boundary layer, provides the illuminating flux. In this energy band, the reflection model parameters are mainly determined by the shape of the iron line and are perfectly compatible with the results described in this work. In other words, the inner disk parameters we obtain for this source under the hypothesis that the line is produced by reflection of the primary Comptonization spectrum on the inner accretion disk, are always compatible with each other, independently of the particular model used to fit the reflection component (such as DISKLINES, REFBB, PEXRIV, REFLIONX, XILLVER).

To support this disk-reflection scenario, all the reflection component should be fitted by a self-consistent reflection model. Unfortunately, no reflection model includes all the reflection features. In the case of REFLIONX, two emission lines are needed to reproduce Ar XVIII and Ca XIX emission lines detected in the soft state. We also needed to add an edge at ∼8.5 keV. To check whether the edge was consistent with a disk origin, we used another reflection model: PEXRIV. The edge is taken into account correctly by this model, but the model does not include any emission line. The XILLVER model includes S, Ar, Ca, and Fe lines, but the addition of an edge at ∼8.5 keV was again necessary to obtain a good fit.

As shown by our analysis, the quality reached by today's observatories is such that it is now compelling to calibrate the reflection broad band spectrum better, because important features are clearly present (like emission lines from low Z-elements) and others are not accounted for well enough (as absorption edges of highly ionized elements).

6.3. The continuum parameters

The main differences between the spectral parameters obtained from the soft and the hard states are discussed in the following. They concern the electron temperature and the seed photon temperature of the Comptonized component, the inner radius of

the disk as derived from the smearing of the reflection component, and the ionization of the reflection component. We note here that we had to fix the parameters of the continuum of the reflection component to the parameters of the NTHCOMP component used to represent the primary Comptonization spectrum. In this case, to obtain a good fit, we had to fix the folding energy parameter to 2.7 times the electron temperature in the soft state and to the electron temperature in the hard state, in agreement with the fact that the peak of a saturated Comptonization spectrum is at 2.7 kT_e, while the peak of an unsaturated Comptonization spectrum is at kT_e.

We observe a clear difference in the spectral parameters from the soft to the hard state. The electron temperature increases from kT_e = 2−3 keV in the soft state to ∼20−24 keV in the hard state, whereas the power-law photon index and the temperature of the seed photons decrease from Γ = 2.2−2.8 to Γ = 1.8 and from kT_{seed} = 1.1−1.4 keV to 0.7−0.8 keV, respectively.

To evaluate the changes in the optical depth and the region of the seed photons from one state to the other, we use the parameters obtained by the NTHCOMP model. This model specifies the Comptonization via the electron temperature in the corona kT_e, the temperature of photons injected in the corona kT_{seed}, and the spectral slope Γ. These parameters are related to the optical depth τ as

$$\Gamma = -\frac{1}{2} + \left[\frac{9}{4} + \frac{1}{\frac{kT_e}{m_e c^2} \tau \left(1 + \frac{\tau}{3}\right)} \right]^{1/2} \quad (1)$$

(Lightman & Zdziarski 1987). We use the values of the NTHCOMP components reported in the first column of Tables 7 and 8, which correspond to the REFLIONX model for the reflection component in both states. The optical depth decreases from the soft to the hard state, from $\tau \sim 7$ to $\tau \sim 3$. Moreover, we

compute the Comptonization parameter y defined by

$$y = 4 \frac{kT_e}{m_e c^2} \times \max(\tau, \tau^2) \qquad (2)$$

and obtain $y \sim 1$ and $y \sim 2$ in the soft and hard states, respectively. To estimate the radius of the emitting region of the seed photons that are Comptonized in the hot corona, we assume their emission as a blackbody and the bolometric Comptonized flux as $F_{Compt} = F_{seed}(1 + y)$ since we have to correct for energy gained by the photons in the inverse Compton scattering. As a result, F_{seed} is defined by

$$F_{seed} = \sigma T_{seed}^4 \left(\frac{R_{seed}}{d} \right)^2, \qquad (3)$$

so the region of the seed photons is obtained by

$$R_{seed} = 3 \times 10^4 d \frac{[F_{Compt}/(1 + y)]^{1/2}}{(kT_{seed})^2} \text{ km} \qquad (4)$$

(see in't Zand et al. 1999) with d the distance in kpc, F_{Compt} in erg cm^{-2} s^{-1}, and kT_{seed} in keV. By considering the F_{Compt} obtained with *BeppoSAX* that is 8.84×10^{-9} and 2.09×10^{-9} erg cm^{-2} s^{-1} in the soft and hard states, respectively, and a distance of 7.4 kpc, we obtain $R_{seed} \sim 9$ km in the soft state and $R_{seed} \sim 12$ km in the hard state, so the seed photons are compatible with coming from the neutron star surface in both states. These results are consistent with a corona above the disk and/or between the disk and with the stellar surface that is hotter in the hard state than in the soft state. This is likely due to the interactions with the soft photons from the disk that are more or less intense depending upon the geometry of the disk-corona system. It can also be connected with the energetic balance between the Compton cooling provided by the soft photons (which acts as the photon number, so with the fourth power of the temperature) and the coronal heating (maybe through shock dissipation).

For the blackbody component, in the soft state kT_{bb} is 0.57 keV. Assuming a distance of 7.4 kpc, the region associated with the blackbody has an apparent radius $\sim R_{bb} = 30$ km, in agreement with the emission coming from the hottest part of the accretion disk, which corresponds to the inner part of the disk close to the neutron star. In the hard state, the blackbody temperature is $kT_{bb} = 0.25$ keV for all the instruments except for *XMM-Newton*, for which $kT_{bb} = 0.57$ keV. The radius associated to the first value is $\sim R_{bb} = 160$ km, again compatible with a truncated accretion disk, whereas the second one is $\sim R_{bb} = 30$ km. It is not clear whether the temperature of the blackbody component changes between the soft and the hard states, since for this parameter we find a very similar value for the hard state to what is found for the soft state for the *XMM-Newton* dataset, while the other instruments suggest a lower value. However, in the hard state, we note similar values of the blackbody normalization for different temperatures. The reason *XMM-Newton* gives a much higher blackbody temperature than *BeppoSAX* and RXTE may be a contamination from the boundary layer emission visible during the *XMM-Newton* observation and not during the other ones (of course the boundary layer emission may be directly visible when it is not completely comptonized in the corona).

6.4. The inclination of the system

The inclination angle of the system with respect to the line of sight, the inner radius of the disk, the emissivity index, and the centroid energy of the line are determined by the profile of the lines (Fabian et al. 1989). These parameters are mutually correlated, and it may be difficult to disentangle their contribution to the overall line shape. For example, as discussed by Cackett et al. (2010), the inclination and the emissivity index play similar roles in determining the line profile. A high value of these parameters makes the line broad and less peaked, so a high value of the inclination and a low value of the emissivity index will give a similar profile to one with a low value of the inclination and a high value of the emissivity index.

In the soft state the observed emission lines, especially the iron line profile, allow us to obtain a good constraint on the inclination angle of the system. Using REFLIONX, we find $i = 35$−$40°$. Applying XILLVER instead of REFLIONX to the data, we obtain $i = 25$−$27°$. (The difference between the best fit values of the inclination angle and the ionization parameter obtained with XILLVER and REFLIONX are caused by the different energy range used to extrapolate the illuminating flux in the two models, Garcia, priv. comm.) However, using other models on the *XMM-Newton* data, which are the best-quality data obtained on 4U 1705−44, such as DISKLINE and PEXRIV, the inclination is found at 38−41°, in agreement with REFLIONX. Because the χ^2/d.o.f. is higher in the case of XILLVER and because all the other models indicate the same range of values for the inclination, we conclude that the inclination of 4U 1705−44 is between 35−41° with respect to the line of sight.

6.5. Geometry of the accretion disk

In all the models, the RDBLUR component was needed to improve the fit. The mildly relativistic blurring was applied to the entire reflection spectrum, confirming the common origin of the reflection features in the inner part of the accretion disk, where strong relativistic effects broaden emission and absorption features. This component gives us information on the inner radius of the accretion disk, $R_{in} = 10$−$16 R_g$ in the soft state, and $R_{in} = 19$−$59 R_g$ ($R_{in} = 26$−$65 R_g$ for the inclination fixed at 39°) in the hard state, so we have an indication that the accretion disk is close to the neutron star surface in the soft state and truncated farther from the compact object in the hard state. This agrees with Barret & Olive (2002) and Olive et al. (2003), who interpret the transitions from one state to the other in this source with different truncation radii of the accretion disk. This is also a possible interpretation for black hole binaries that show clearer transitions from the soft to the hard state and vice versa (e.g. Done et al. 2007).

The spectral state transitions are also associated with variations in the overall X-ray luminosity. We calculated the accretion rate in both states using the typical value of the accretion efficiency $\eta = 0.2$, corresponding to a neutron star ($M_{NS} = 1.4 M_\odot$ and $R_{NS} = 10$ km), and to the bolometric luminosities inferred by our spectral modeling. In the soft state, $\dot{M}_{SS} = 1.6 \times 10^{-8} M_\odot$ yr^{-1}, while in the hard state the accretion rate decreases, $\dot{M}_{HS} = 2 \times 10^{-9} M_\odot$ yr^{-1}. This difference in the accretion rate is consistent with changes in the flow geometry, hence with a different inner radius of the accretion disk. The evaporation of the inner part of the accretion disk may lead to a truncated disk at low-mass accretion rates (e.g. Meyer et al. 2000).

We therefore infer a similar geometry to what has been proposed for black hole binaries where the accretion disk is truncated at low luminosity (Barrio et al. 2003; Done & Diaz Trigo 2010); however, some differences should be observed between these systems, especially in the soft state, because of the boundary layer in the case of the neutron star binaries. And in fact we

find that the disk is truncated in 4U 1705−44 relatively far from the compact object (at more than $10\,R_{\rm g}$ both in the soft and in the hard state) as is inferred by the fact that the observed distortion of the iron line profile is never extreme.

6.6. The ionization parameter

Reflection models give an indication of the ionization state of the matter in the inner part of the accretion disk: $\xi = 4\pi F_{\rm X}/n_{\rm H}$, where $F_{\rm X}$ is the total illuminating flux (erg cm^{-2} s^{-1}) and $n_{\rm H}$ is the hydrogen number density. We note that the matter is much more ionized in the soft state, $\xi = 3600$ erg cm s^{-1}, in comparison with $\xi = 210$ erg cm s^{-1} in the hard state. This again agrees with the disk-reflection scenario for a truncated disk and with a lower illuminating flux in the hard state. When the accretion rate is high, the disk penetrates the hot flow, favoring the interactions between the inner disk and the illuminating flux and resulting in a high ionization and of the matter in the disk and, possibly, in a high reflection amplitude (e.g. Poutanen et al. 1997). In contrast, when the accretion rate is low, the disk is truncated farther from the compact object, disk matter is less ionized, and the amount of reflection is intrinsically low (e.g. Barrio et al. 2003). This is consistent with the observed energy of the iron line found in the soft state, $E_{\rm Fe} = 6.6$–6.7 keV, and in the hard state, $E_{\rm Fe} = 6.4$–6.5 keV (see also Reis et al. 2009b, who emphasize the influence of the ionization state of the accretion disk on the iron line profile).

6.7. Overabundance of some elements

Determination of the abundances of heavy elements is important for inferring how they originated. Most heavy elements from Si to Fe develop from explosive nucleosynthesis in supernovae. Type Ia supernovae, which correspond to the explosion of an accreting white dwarf in a binary system when its mass becomes superior to $1.4\,M_{\odot}$ via mass transfer, mainly provide Fe, whereas core collapse supernovae (SN II, Ib, IIb) associated to the gravitational collapse of the iron core of a massive star after successive stages of hydrostatic burning, provide intermediate elements, from Si to Ca.

In the soft state of 4U 1705−44, *XMM-Newton* detected emission lines corresponding to S, Ca, Ar, and Fe. Using reflection models we have investigated a possible overabundance of some elements with respect to their solar abundance. Applying REFLIONX we have an indication of an iron overabundance by a factor 2−3, probably responsible for the apparent large edge observed in the soft state (Ross & Fabian 2005). This result agrees with D'Aì et al. (2010), who evaluated the iron overbundance by a factor ∼3 by using REFBB, in addition to an overabundance of S with respect to the other elements (or solar abundance).

In the hard state, the lower statistics do not allow us to detect other emission lines than Fe, so it is difficult to estimate any overabundance. When this parameter (Fe/sol) is free to vary in REFLIONX, its value is close to 1, and the inner radius of the disk is found at about $R_{\rm in} = 19$–$59\,R_{\rm g}$. When we fix the abundance of iron to a factor 2 with respect to the solar abundance, the inner radius is found at a slightly greater distance from the neutron star $R_{\rm in} = 24$–$79\,R_{\rm g}$, confirming the evidence of a truncated disk in the hard state. It is therefore important to obtain good constraints on the abundance of Fe and other elements, if possible, because this parameter also has a direct effect on the estimate of the inner radius of the disk.

6.8. Comparison with Cyg X-2 and GX 3+1

Both Cygnus X-2 and GX 3+1 are bright neutron star LMXBs showing spectral features similar to those observed in 4U 1705−44. The Z-source Cyg X-2 is one of the rare persistent LMXB whose secondary star is easily observed. It appears to be a high-inclination system ($i > 60°$) since short-duration dips have been detected in its light curve (Vrtilek et al. 1988; Orosz & Kuulkers 1999). The width of the brightest spectral lines of Mg XII, Si XIV, S XVI, Fe XXV, and Fe XXVI resolved by Chandra indicate velocity dispersion ranging from 1000 to 3000 km s^{-1} (Schulz et al. 2009), and they are consistent with a stationary, dense, and hot accretion-disk corona. Moreover, a *Suzaku* observation reveals the presence of a red-skewed wing of the Kα iron line in this source (Shaposhnikov et al. 2009), possibly explained by reflection of X-ray radiation from a cold accretion disk or by Compton down-scattering in a mildly relativistic wind outflow (Laurent & Titarchuk 2007). In the case of 4U 1705−44, the observed emission lines could not be resolved into blending of different lines, whether with *XMM-Newton* (Di Salvo et al. 2009) or with the *Chandra* High Energy Transmission Grating (Di Salvo et al. 2005). We infer velocities associated with the different emission lines of ∼11 000 km s^{-1} ($E_{\rm Fe} = 6.69 \pm 0.01$ keV, $\sigma_{\rm Fe} \sim 0.25$ keV; $E_{\rm Ar} = 3.31 \pm 0.02$ keV, $\sigma_{\rm Ar} \sim 0.13$ keV) and a red-skewed Kα iron line, with a line width similar to the one observed in Cyg X-2 ($\sigma_{\rm Fe} \sim 0.22$–$0.25$ keV). In both sources, the intercombination line dominates the Fe XXV triplet. However, the width measured for the 6.68 keV line is much more in 4U 1705−44 than in the case of the *Chandra* observation of Cyg X-2, but it is similar to the line width measured in the *Suzaku* observation of Cyg X-2. Because of the lower statistics of Chandra grating spectra, it may be possible that the red wing of the line is not easily observed by Chandra and is better detected by the large-area instruments of *Suzaku* and *XMM-Newton*.

Another peculiar system presenting very similar features to those observed in 4U 1705−44 is the type-I X-ray burster GX 3+1. Recently, a broad and asymmetric iron line, in addition to Ar XVIII and Ca XIX lines, has been detected with *XMM-Newton* in this persistent and bright atoll source (Piraino et al. 2012). The iron line profile is well fitted by a relativistically smeared profile and is thought to come from reflection in the inner parts of the accretion disk. As in 4U 1705−44, the line profile does not depend upon the photon pile-up fraction in the EPIC-pn spectrum, in agreement with Miller et al. (2010). The parameters obtained from the line profile modeled with a Gaussian or a diskline, such as the emission line width, the inclination of the system with respect to the line of sight, $35° < i < 44°$, and the inner disk radius, are remarkably similar to those we find for 4U 1705−44, indicating similar geometry and physical parameters of the disk-corona system in these bright sources.

7. Conclusions

Reflection features present complex profiles that mainly depend on the relativistic blurring, caused by Doppler effects of the high Keplerian velocities and, possibly, gravitational redshift at the inner disk radius, on the incident flux, on the ionization state of the matter in the disk, on the abundance of the elements, and on the inclination of the system with respect to the line of sight. The study of these features gives invaluable information on the system. We performed a broad band (0.4−200 keV) and moderately high-energy resolution spectral analysis of the X-ray burster 4U 1705−44 both in the soft and in the hard states using data

from *XMM-Newton*, *BeppoSAX*, and RXTE observatories. This source is particularly interesting since it shows several reflection features observed at a high S/N. We fitted these features with several self-consistent reflection models in order to test the common origin of all these features, which are all compatible with being produced by reflection of the primary Comptonization spectrum on the inner accretion disk. In this scenario we inferred the main parameters of the inner accretion disk. In particular, we found (i) the inclination of the system with respect to the line of sight that is constrained in the range 35−41°, (ii) the inner radius of the disk that increases from 10−16 R_g in the soft state up to 26−65 R_g in the hard state, and (iii) the ionization parameter that decreases from ~3600 erg cm s^{-1} in the soft state to 210 erg cm s^{-1} in the hard state. We also find an indication of an iron overabundance by a factor 2−3 with respect to its solar abundance. All these results appear to be strong against the particular reflection model used to fit these features and against possible distortion caused by photon pile-up in the *XMM-Newton*/EPIC-pn CCDs.

We have also discussed the differences in the spectral parameters between the soft and the hard states. The results found are consistent with the following scenario. At low luminosity, the accretion disk is truncated farther from the neutron star, so the interaction efficiency of the disk photons with the hot electrons of the corona is lower. The rate of photons coming from the disk is also lower because of the cooler temperature of the disk. This results in a hard spectrum and a low-ionization reflection. At higher luminosity, the mass accretion rate increases and the inner radius of the disk moves closer to the compact object. The soft photons from the disk are much more efficient at cooling the corona, resulting in a softer spectrum. In addition to this, reflection increases due to a stronger irradiation of the disk, and the matter becomes more ionized. Moreover, the emission lines are broadened by stronger Doppler effects as the disk approaches the compact object.

This scenario is generally well supported by the timing analysis through power density spectra where correlations are observed between the characteristic frequencies of the fast time variability and the position of the source in the CD or in its spectral state (e.g. Olive et al. 2003), with characteristic frequencies increasing when increasing the inferred mass accretion rate.

Appendix A: Pile-up

The task EPATPLOT offers the possibility to check whether an observation suffers from pile-up. Here we compare the following different cases, when all the columns of the CCD are used (pn-all), when the brightest central column is excluded (pn-1), when the two brightest central columns are excluded (pn-2), and finally when the seven brightest columns are excluded (pn-7, as proposed by Ng et al. 2010) in order to determine if the 4U 1705−44 spectra were affected by significant pile-up during the *XMM-Newton* observation in the soft state. We note the presence of some pile-up below 2 keV and above 10 keV, unless 7 central columns are excluded. We specify that we have restricted our spectral analysis between 2.4 and 11 keV, which is the range of interest for the study of the iron Kα line complex.
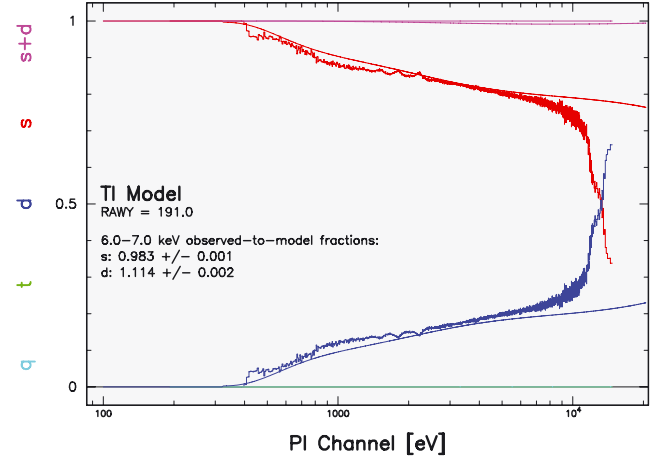
Fig. A.1. Estimation of the pile-up fraction in the EPIC-pn through the epatplot tool at the 6−7 keV iron line energy range when all the columns of the CCD are considered. The plot represents the spectra of the single (red) and double (blue) events. Solid lines indicate the expected fraction from the model curves.
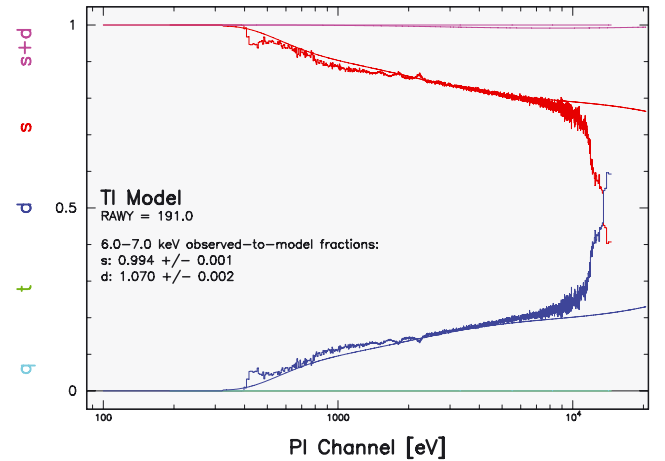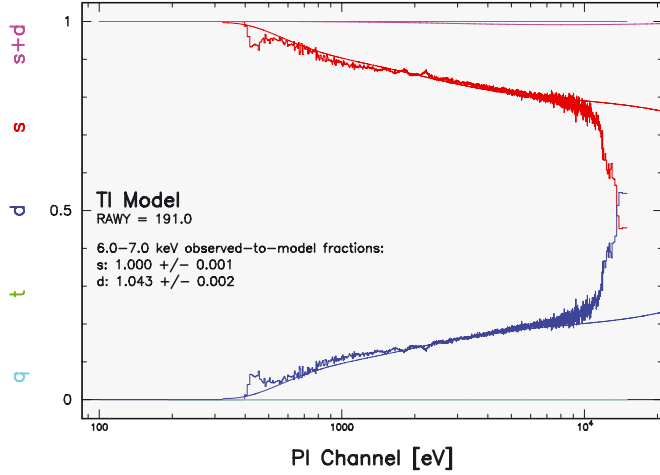

Fig. A.2. Same as in Fig. A.1 for pn-1, in which the brightest central column of the CCD has been excluded.

Moreover, it is possible to quantify the amount of pile-up in a given energy range. By default this range is from 0.5 to 2 keV, which corresponds to the softest part of the spectrum, which is where it is the most sensitive to pile-up. We estimate the amount of pile-up in the energy band of the iron emission line (6−7 keV).

When we use all the columns of the CCD, we note a deviation between the observed and the expected distribution that testifies to the presence of pile-up in the spectrum (Fig. A.1). The observed-to-model fractions of the single and double are 0.98 and 1.11, respectively, in the 6−7 keV band. If we exclude the central column, the deviation is less important, especially for the single events (Fig. A.2). The observed-to-model fractions corresponding to the single and double events are 0.99 and 1.07. When we exclude two central columns, the single and double distributions follow the expected models, meaning that the observation no longer suffers from pile-up (Fig. A.3). The corresponding ratios are 1.00 and 1.04. Finally we exclude the seven brightest columns. The single and double distributions are overestimated in comparison to the models (Fig. A.4). The associated ratios are 1.03 and 0.91, respectively, in the 6−7 keV energy band. We therefore conclude that the best solution is to exclude two central columns of the CCD in order to avoid pile-up and to have the most correct distribution of single and double events at

Fig. A.3. Same as in Fig. A.1 for pn-2, in which the 2 brightest central columns of the CCD have been excluded.
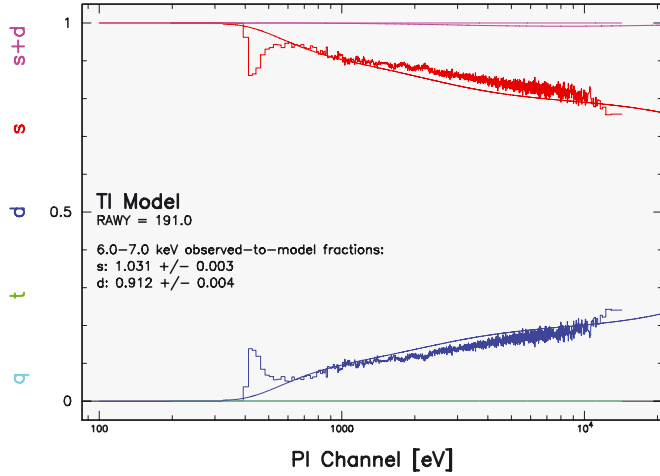
Fig. A.4. Same as in Fig. A.1 for pn-7, in which the 7 brightest central columns of the CCD have been excluded.

the iron-line energy band. Note also that the range below 2 keV is covered by the RGS, and it is therefore not necessary to eliminate more central columns in the pn CCD with the aim to reduce the pile-up fraction below 2 keV. In other words, we prefer to exclude from our spectral analysis the softer energy range in the pn spectrum, which is covered by the RGS, in order to maximize the statistics of the pn spectrum and the quality of the instrumental response reconstruction in the range of interest for iron line studies.

References

Anders, E., & Grevesse, N. 1989, Geochim. Cosmochim. Acta, 53, 197
Arnaud, K. A. 1996, in Astronomical Data Analysis Software and Systems V, ASP Conf. Ser., 101, 17
Ballantyne, D. R. 2004, MNRAS, 351, 57
Ballantyne, D. R., Ross, R. R., & Fabian, A. C. 2001, MNRAS, 327, 10
Balucinska-Church, M., & McCammon, D. 1992, ApJ, 400, L699
Barret, D., & Olive, J. F. 2002, ApJ, 576, 391

Barrio, F. E., Done, C., & Nayakshin, S. 2003, MNRAS, 342, 557
Cackett, E. M., Miller, J. M., Ballantyne, D. R., et al. 2010, ApJ, 720, L205
Cackett, E. M., Miller, J. M., Reis, R. C., Fabian, A. C., & Barret, D. 2012, ApJ, 755, 27
D'Aì, A., Iaria, R., Di Salvo, T., Matt, G., & Robba, N. R. 2009, ApJ, 693, L1
D'Aì, A., Di Salvo, T., Ballantyne, D., et al. 2010, A&A, 516, A36
Di Salvo, T., Iaria, R., Mendez, M., et al. 2005, ApJ, 623, L121
Di Salvo, T., D'Aì, A., Iaria, R., et al. 2009, MNRAS, 398, 2022
Done, C., & Diaz Trigo, M. 2010, MNRAS, 407, 2287
Done, C., Gierlinski, M., & Kubota, A. 2007, A&ARv, 15, 1
Egron, E., Di Salvo, T., Burderi, L., et al. 2011, A&A, 530, A99
Fabian, A. C., & Miniutti, G. 2005 (Cambridge Univ. Press) [arXiv:astro-ph/0507409]
Fabian, A. C., Rees, M. J., Stella, L., & White, N. E. 1989, MNRAS, 238, 729
Fabian, A. C., Iwasawa, K., Reynolds, C. S., & Young, A. J. 2000, PASP, 112, 1145
Fabian, A. C., Zoghbi, A., Ross, R. R., et al. 2009, Nature, 459, 540
Fiocchi, M., Bazzano, A. P. U., & Zdziarski, A. A. 2007, ApJ, 657, 448
Ford, E., van der Klis, M., & Kaaret, P. 1998, ApJ, 498, L41
Forman, W., Jones, C., Cominsky, L., et al. 1978, ApJ, 38, 357
Galloway, D. K., Muno, M. P., Hartman, J. M., Psaltis, D., & Chakrabarty, D. 2008, ApJ, 179, 360
Garcia, J., & Kallman, T. R. 2010, ApJ, 718, 695
George, I. M., & Fabian, A. C. 1991, MNRAS, 249, 352
Hasinger, G., & van der Klis, M. 1989, A&A, 225, 79
Iaria, R. and D'Aì, A., di Salvo, T., et al. 2009, A&A, 505, 1143
in't Zand, J. J. M., Verbunt, F., Strohmayer, T. E., et al. 1999, A&A, 345, 100
Kaastra, J. S., & Mewe, R. 1993, A&AS, 97, 443
Kallman, T., & White, N. E. 1989, ApJ, 341, 955
Langmeier, A., Sztajno, M., Hasinger, G., Truemper, J., & Gottwald, M. 1987, ApJ, 323, 288
Laor, A. 1991, ApJ, 376, 90
Laurent, P., & Titarchuk, L. 2007, ApJ, 656, 1056
Lightman, A. P., & Zdziarski. 1987, ApJ, 319, 643
Lin, D., Remillard, R. A., & Homan, J. 2010, ApJ, 719, 1350
Maccarone, T. J. 2012 [arXiv:1204.3154]
Magdziarz, P., & Zdziarski, A. A. 1995, MNRAS, 273, 837
Markoff, S., & Nowak, M. 2004, ApJ, 609, 972
Markoff, S., Nowak, M., & Wilms, J. 2005, ApJ, 635, 1203
Martocchia, S., & Matt, G. 1996, MNRAS, 282, L53
Matt, G. 2006, AN, 327, A96
Meyer, F., Liu, B. F., & Meyer-Hofmeister, E. 2000, A&A, 361, 175
Miller, J. M., D'Aì, A., Bautz, M. W., et al. 2010, ApJ, 724, 1441
Ng, C., Diaz Trigo, M., Cadolle Bel, M., & Migliari, S. 2010, A&A, 522, A96
Olive, J. F., & Barret, D. M. G. 2003, ApJ, 583, 416
Orosz, J. A., & Kuulkers, E. 1999, MNRAS, 305, 132
Papitto, A., Riggio, A., Di Salvo, T., et al. 2010, MNRAS, 407, 2575
Piraino, S., Santangelo, A., Di Salvo, T., et al. 2007, A&A, 471, L17
Piraino, S., Santangelo, A., Kaaret, P., et al. 2012, A&A, 542, L27
Poutanen, J., & Svensson, R. 1996, ApJ, 470, 249
Poutanen, J., Krolik, J. H., & Ryde, F. 1997, MNRAS, 292, L21
Reis, R. C., Fabian, A. C., Ross, R. R., & Miller, J. M. 2009a, MNRAS, 395, L1257
Reis, R. C., Fabian, A. C., & Young, A. J. 2009b, MNRAS, 399, L1
Reynolds, C. S., & Nowak, M. A. 2003, Phys. Rep., 377, 389
Ross, R. R., & Fabian, A. C. 2005, MNRAS, 358, 211
Ross, R. R., & Fabian, A. C. 2007, MNRAS, 381, 1697
Schulz, N. S., Huenemoerder, D. P., Ji, L., et al. 2009, ApJ, 692, L80
Shaposhnikov, N., Titarchuk, L., & Laurent, P. 2009, ApJ, 699, 1223
Titarchuk, L., Laurent, P., & Shaposhnikov, N. 2009, ApJ, 700, 1831
Vrtilek, S. D., Swank, J. H., Kelley, R. L., & Kahn, S. M. 1988, ApJ, 329, 276
Vrtilek, S. D., Soker, N., & Raymond, J. C. 1993, ApJ, 404, 696
Walton, D. J., Reis, R. C., Cackett, E. M., Fabian, A. C., & Miller, J. M. 2012, MNRAS, 422, 2510
White, N. E., & Holt, S. S. 1982, ApJ, 257, 318
White, N. E., Peacock, A., Hasinger, G., et al. 1986, ApJ, 218, 129
Yan, M., Sadeghpour, H. R., & Dalgarno, A. 1998, ApJ, 496, L1044
Zdziarski, A. A., Johnson, W. N., & Magdziarz, P. 1996, MNRAS, 283, 193
Zycki, P. T., Done, C., & Smith, D. A. 1999, MNRAS, 309, 561